

Ionized filaments and ongoing physical processes in massive star-forming sites around $l = 345.5$ degree

L. K. Dewangan¹★, L. E. Pirogov², N. K. Bhadari^{1,3}, and A. K. Maity^{1,3}

¹Physical Research Laboratory, Navrangpura, Ahmedabad - 380 009, India.

²Institute of Applied Physics of the Russian Academy of Sciences, 46 Ulyanov st., Nizhny Novgorod 603950, Russia.

³Indian Institute of Technology Gandhinagar Palaj, Gandhinagar 382355, India.

ABSTRACT

Numerous research studies on dust and molecular filaments have been conducted in star-forming sites, but only a limited number of studies have focused on ionized filaments. To observationally study this aspect, we present an analysis of multi-wavelength data of an area of $\sim 74'.6 \times 55'$ around $l = 345^\circ.5$. Using the 843 MHz continuum map, two distinct ionized filaments (i.e., IF-A (extent $\sim 8'.5$) and IF-B (extent $\sim 22'.65$)) hosting ionized clumps powered by massive OB stars are identified. Using the $^{13}\text{CO}(2-1)$ and $\text{C}^{18}\text{O}(2-1)$ line data, the parent molecular clouds of IF-A and IF-B are studied in a velocity range of $[-21, -10] \text{ km s}^{-1}$, and have filamentary appearances. At least two cloud components around -18 and -15 km s^{-1} toward the parent clouds of IF-A and IF-B are investigated, and are connected in velocity space. These filamentary clouds also spatially overlap with each other along the major axis, backing the filamentary twisting/coupling nature. Noticeable Class I protostars and massive stars appear to be observed toward the common zones of the cloud components. These findings support the collision of two filamentary clouds around 1.2 Myr ago. The existence of the ionized filaments seems to be explained by the combined feedback of massive stars. The molecular filaments associated with IF-A and IF-B favour the outcomes of the most recent model concerning the escape and the trap of the ionizing radiation from an O star formed in a filament.

Key words: dust, extinction – HII regions – ISM: clouds – ISM: individual object (IRAS 17008-4040, IRAS 17009-4042, S11, and IRAS 17028-4050) – stars: formation – stars: pre-main sequence

1 INTRODUCTION

In recent years, sub-millimeter(mm) continuum and molecular-line studies have revealed molecular and dust filaments as common features in massive star-forming regions (e.g., André et al. 2010, 2014; Treviño-Morales et al. 2019). The involvement of these filaments in the study of the origin of massive OB-stars ($M \gtrsim 8 M_\odot$) has received great impetus in recent years. In other words, multi-scale and multi-wavelength studies of the filaments are a reliable approach to deepen understanding of massive star formation (MSF) mechanisms. It has been thought that OB stars are assembled by large-scale (1–10 pc) inflow material that may be funneled along filaments (e.g., Tan et al. 2014; Motte et al. 2018; Hirota 2018; Rosen et al. 2020). Such process favours the convergence of filaments toward the compact and dense hub, or a star-forming clump surrounded by filaments or a junction of filaments (i.e., hub-filament system (HFS); Myers 2009; Motte et al. 2018). A hub-filament configuration is almost universally detected in massive star-forming regions. Furthermore, the intersection/merging/collision of filaments can also explain the formation of massive OB stars and stellar clusters (e.g., Habe &

Ohta 1992; Anathpindika 2010; Fukui et al. 2021, and references therein). Hence, multiple physical processes are expected to be operated in massive star-forming regions.

Apart from the molecular and dust filaments, one may also expect elongated filaments of ionized gas in star-forming regions, but such study is very limited in the literature (e.g., LBN 140.07+01.64 (Karr & Martin 2003; Dewangan et al. 2021); Eridanus filaments (Pon et al. 2014); Cygnus X (Emig et al. 2022)). Hence, the simultaneous study of the ionized, dust, and molecular filaments is still lacking due to scarcity of the ionized filaments in star-forming regions (e.g., LBN 140.07+01.64; Dewangan et al. 2021). The ionizing radiation from OB-association (or OB-star complex) is thought to be responsible for the origin of ionized filaments. Such ionized filaments are found at far distances from the exciting stars/complex (e.g., Karr & Martin 2003; Pon et al. 2014; Emig et al. 2022). On the other hand, there is a possibility that several massive stars formed in molecular/dust filamentary clouds may locally produce the ionized filaments in the same clouds. However, such a proposal is yet to be explored in star-forming sites. Hence, such targets offer to study not only the birth of massive OB stars, but also the origin of elongated ionized filaments. It also enables us to study the role of filaments in

★ lokeshd@prl.res.in

MSF activities and the impact of massive OB stars on their parent filaments.

In this context, the present paper deals with a wide target area around $l = 345^\circ.5$, which contains several star-forming sites (e.g., IRAS 17008-4040, IRAS 17009-4042, IRAS 17006-4037, IRAS 17028-4050, IRAS 17027-4100, IRAS 17026-4053, and IRAS 17024-4106). Among these highlighted sources, IRAS 17008-4040 and IRAS 17009-4042 are well known massive star-forming regions. The selected target area is not very distant (< 2.5 kpc), and hosts previously known H II regions powered by massive OB stars, dust filaments, clusters of young protostars, and a massive protostar in a young, pre-ultracompact H II phase. The selected sources are the potential targets to explore the role of filaments in MSF processes and the impact of massive stars on the filaments. Furthermore, such targets also seem to be very promising for investigating the ionized filaments and their molecular environments, which is a very poorly studied topic in star formation research.

Situated at a distance of ~ 2.4 kpc, the sites IRAS 17008-4040 (hereafter i17008) and IRAS 17009-4042 (hereafter i17009) are associated with H II regions powered by B-type stars (Garay et al. 2006, 2007; Dewangan et al. 2018c). Radio continuum morphologies of the H II regions at different radio frequencies (i.e., 0.61, 1.28, 1.4, and 2.5 GHz) were examined by Dewangan et al. (2018c) (see Figure 9 in their paper). An elongated filament hosting the sites i17008 and i17009 was reported using the APEX Telescope Large Area Survey of the Galaxy (ATLASGAL; Schuller et al. 2009) 870 μm continuum map (see also Dewangan et al. 2018c). With the aid of the 870 μm continuum data, at least one dust continuum clump is detected toward these two IRAS sites. Clumps clm1 ($M_{\text{clump}} \sim 2430 M_\odot$; $T_d \sim 30$ K; $V_{\text{lsr}} = -17$ km s $^{-1}$; $d \sim 2.4$ kpc) and clm2 ($M_{\text{clump}} \sim 2900 M_\odot$; $T_d \sim 27.3$ K; $V_{\text{lsr}} = -17.3$ km s $^{-1}$; $d \sim 2.4$ kpc) are detected toward i17008 and i17009, respectively (see Urquhart et al. 2018; Dewangan et al. 2018c, for more details). The study of the *Herschel* sub-mm maps revealed the existence of several parsec-scale filaments directed toward the dust clump hosting each IRAS site, exhibiting HFS candidates (Dewangan et al. 2018c). Additionally, the site i17008 hosts an infrared counterpart (IRc) of the 6.7 GHz methanol maser emission (MME), which is also associated with an extended green object (EGO; Cyganowski et al. 2008). The IRc has been proposed as an O-star candidate without an H II region (see Figure 9 in Dewangan et al. 2018c), which drives an outflow (Cyganowski et al. 2008; Morales et al. 2009; Dewangan et al. 2018c). Overall, the ongoing star formation activities (including massive stars) were reported toward i17008 and i17009 using the infrared photometric data and radio continuum maps (Dewangan et al. 2018c).

Figures 1a and 1b present the radio continuum emission contours at 843 MHz from the Sydney University Molonglo Sky Survey (SUMSS; Bock et al. 1999) and the *Spitzer* Galactic Legacy Infrared Mid-Plane Survey Extraordinaire (GLIMPSE; Benjamin et al. 2003) 8.0 μm image of a wide area (size $\sim 74'.64 \times 55'.02$; centered at $l = 345^\circ.3693$; $b = 0^\circ.0391$), respectively, which is the target area of this paper. At least two elongated morphologies or ionized filaments appear in the 843 MHz continuum map toward our selected area around $l = 345^\circ.5$ (see two dotted-dashed boxes in Figure 1a), where the extended emission in the 8.0 μm image is also traced (see Figure 1b and also Section 3.1.1 for more details). We do not find any study of these elongated ionized filaments in the literature as well as their association with the dust and molecular filaments.

There is no understanding of the existence of these structures and of the ongoing physical mechanisms around $l = 345^\circ.5$. In this

context, to observationally study the formation of massive stars and the origin of the ionized filaments, an extensive analysis of the multi-wavelength data sets (see Section 2) is performed. In particular, to study the parent molecular clouds of the ionized filaments, we analyzed the unexplored molecular line data from the structure, excitation, and dynamics of the inner Galactic interstellar medium (SEDIGISM; Schuller et al. 2017, 2021) and the Mopra Southern Galactic Plane CO Survey (Braiding et al. 2018).

Section 2 presents the observational data sets discussed in this paper. The outcomes of this paper are given in Section 3. In Section 4, the implications of our observed outcomes are discussed. Finally, Section 5 gives the conclusions of this study.

2 DATA SETS

The data sets utilized in this work are listed in Table 1, and were obtained toward our selected area around $l = 345^\circ.5$ as presented in Figure 1a. In this paper, we used the Gaia early data release 3 (EDR3; Gaia Collaboration et al. 2021; Fabricius et al. 2021) based photogeometric distances (“rpgeo”) of point-like sources from Bailer-Jones et al. (2021). Based on the analysis of the *Herschel* continuum images at 70–500 μm (Molinari et al. 2010b), the *Herschel* temperature and column density maps (resolution $\sim 12''$) were constructed for the *EU-funded ViaLactea project* (Molinari et al. 2010a). The Bayesian PPMAP procedure (Marsh et al. 2015, 2017) was applied to obtain these *Herschel* maps. The *Herschel* temperature map is used in this paper.

The SEDIGISM $^{13}\text{CO}/\text{C}^{18}\text{O}(J = 2-1)$ line data (beam size $\sim 30''$; pixel-scale $\sim 9''.5$; rms $\sim 0.8-1.0$ K; Schuller et al. 2017, 2021) and the Mopra $^{13}\text{CO}(J = 1-0)$ line data (beam size $\sim 36''$; pixel-scale $\sim 30''$; rms ~ 0.5 K; Braiding et al. 2018) are examined in this paper. These line data were smoothed with a Gaussian function having a width of 3 pixels. The smoothing process gives the resultant angular resolutions of the SEDIGISM $^{13}\text{CO}/\text{C}^{18}\text{O}(J = 2-1)$ line data and Mopra $^{13}\text{CO}(J = 1-0)$ line data to be $\sim 41''.4$ and $\sim 96''.9$, respectively. The Mopra $^{13}\text{CO}(J = 1-0)$ line data are not available for our entire selected target area, but these observations (i.e., $\sim 60'.6 \times 54'.9$; centered at $l = 345^\circ.4801$; $b = 0^\circ.0442$) cover both the ionized filaments. Apart from the $^{13}\text{CO}/\text{C}^{18}\text{O}$ line data, we also studied the $\text{N}_2\text{H}^+(1-0)$ line data from the MALT90 survey (beam size $\sim 38''$; rms ~ 0.2 K; Foster et al. 2011; Jackson et al. 2013) mainly toward i17008 and i17009.

3 RESULTS

3.1 Physical environments around $l = 345^\circ.5$

This section focuses to probe the distribution of dust emission, clumps, ionized emission, molecular gas, and embedded protostars around $l = 345^\circ.5$, which allows us to identify various emission structures, their physical association, and signatures of star formation. Such an investigation is very useful to probe the physical conditions around $l = 345^\circ.5$.

3.1.1 Ionized clumps toward elongated ionized filaments

In order to explore the ionized clumps/H II regions and the ionized filaments, we have employed the radio 843 MHz continuum map in the direction of our selected area around $l = 345^\circ.5$. As mentioned earlier, the spatial appearance of the 843 MHz continuum emission enabled us to trace two elongated ionized filaments

Table 1. List of observational surveys utilized in this work.

Survey	Wavelength/Frequency/line(s)	Resolution (")	Reference
SUMSS	843 MHz	~45	Bock et al. (1999)
SEDIGISM	$^{13}\text{CO}/\text{C}^{18}\text{O}$ ($J = 2-1$)	~30	Schuller et al. (2017)
Mopra Galactic Plane CO survey	$^{12}\text{CO}/^{13}\text{CO}/\text{C}^{18}\text{O}$ ($J = 1-0$)	~36	Braiding et al. (2018)
Millimeter Astronomy Legacy Team Survey at 90 GHz (MALT90)	molecular lines near 90 GHz	~38	Jackson et al. (2013)
ATLASGAL	870 μm	~19.2	Schuller et al. (2009)
Herschel Infrared Galactic Plane Survey (Hi-GAL)	70–500 μm	~5.8–37	Molinari et al. (2010b)
Spitzer MIPS Inner Galactic Plane Survey (MIPSGAL)	24 μm	~6	Carey et al. (2005)
Wide Field Infrared Survey Explorer (WISE)	12 μm	~6	Wright et al. (2010)
Spitzer-GLIMPSE	3.6–8.0 μm	~2	Benjamin et al. (2003)

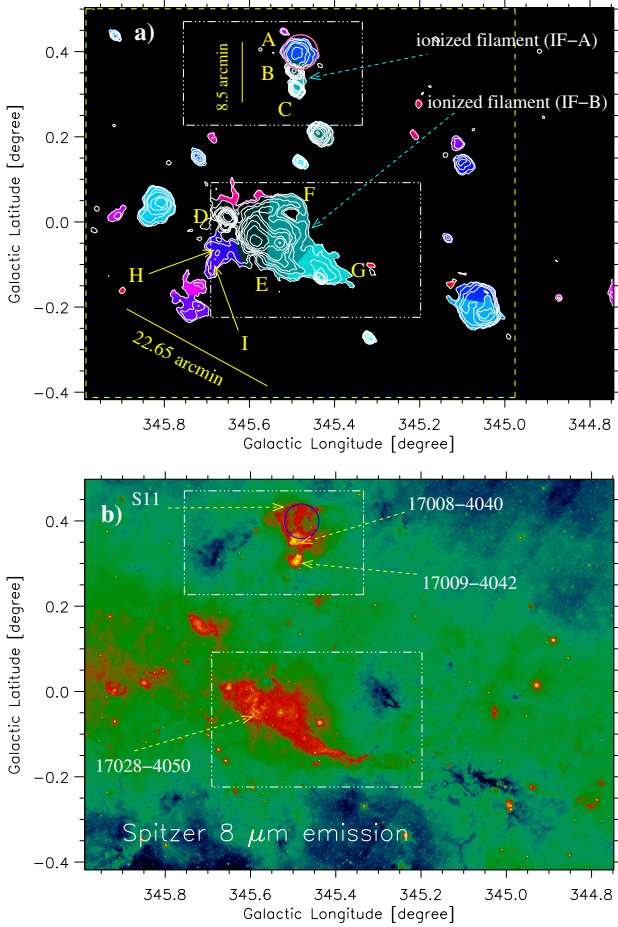
SUMSS 843 MHz continuum emission contours + ionized clumps

Figure 1. a) The panel shows the SUMSS 843 MHz radio continuum contours toward an area of $\sim 74'.64 \times 55'.02$ (centered at $l = 345^\circ.3693$; $b = 0^\circ.0391$). The radio continuum contours are plotted with the levels of 13, 20, 40, 60, 100, 130, 200, 300, and 550 mJy beam $^{-1}$. The background map displays a clumpfind decomposition of the 843 MHz continuum emission, highlighting the spatial boundary of ionized clumps. A dashed box highlights an area presented in Figures 2a–2d. b) The panel presents the *Spitzer* image at 8.0 μm . A big circle shows the location of the MIR bubble S11 (average radius $\sim 2'.43$) in both panels. In each panel, two dotted-dashed boxes highlight areas hosting elongated morphologies.

around $l = 345^\circ.5$ (see Figure 1a), which are designated as IF-A (extent $\sim 8'.5$) and IF-B (extent $\sim 22'.65$). In Figure 1b, the extended emission traced in the 8.0 μm image can be also observed toward both the ionized filaments. The locations of at least three IRAS sources (i.e., i17008, i17009, and IRAS 17028-4050) and a previously known mid-infrared (MIR) bubble S11 ($l = 345^\circ.48$; $b = 0^\circ.399$; Churchwell et al. 2006) are indicated in Figure 1b. The ionized filament IF-A, hosting i17008, i17009, and the bubble S11 is traced in the northern direction, while the filament IF-B is depicted in the southern direction.

In Figures 1a and 1b, the location of the bubble S11 is also marked by a circle (average radius = $2'.43$). This bubble (distance ~ 2.0 kpc; Watson et al. 2010) was identified as a complete/closed ring or a probable enclosed central star cluster with an average radius and thickness of $2'.43$ and $0'.39$, respectively (see Churchwell et al. 2006; Hanaoka et al. 2020). From the previous work of Dewangan et al. (2018c), we find one ATLASGAL dust continuum clump at 870 μm (i.e., clm3; $M_{\text{clump}} \sim 600 M_\odot$; $T_d \sim 16.5$ K; $V_{\text{lsr}} = -15.8$ km s $^{-1}$; $d \sim 2.4$ kpc; see also Urquhart et al. 2018) toward the bubble S11. Based on the previously reported V_{lsr} values toward the dust clumps associated with i17008 and i17009 (i.e., clm1 ($V_{\text{lsr}} = -17$ km s $^{-1}$) and clm2 ($V_{\text{lsr}} = -17.3$ km s $^{-1}$)), we may suggest that the clump clm3 ($V_{\text{lsr}} = -15.8$ km s $^{-1}$) appears to be redshifted compared to the other two clumps. But, it requires further investigation using molecular line data.

In addition to the elongated ionized structures, several peaks are visually seen in the radio continuum map. Hence, we employed the *clumpfind* IDL program (Williams et al. 1994) to identify the ionized clumps/H II regions from the SUMSS 843 MHz continuum map. The *clumpfind* program also allows us to obtain the total flux density (S_ν) of each selected ionized clump/H II region. However, we have labeled nine ionized clumps (i.e., A–I), which are distributed mainly toward IF-A and IF-B (see Figure 1a). In the direction of IF-A, the ionized clumps A, B, and C are found toward the bubble S11, i17008, and i17009, respectively. Six ionized clumps (i.e., D–I) are labeled toward IF-B. In general, the observed flux value is used to compute the number of Lyman continuum photons N_{UV} of an ionized clump/H II region, and in this relation, one can use the following equation (Matsakis et al. 1976):

$$N_{\text{UV}}(s^{-1}) = 7.5 \times 10^{46} \left(\frac{S_\nu}{\text{Jy}} \right) \left(\frac{D}{\text{kpc}} \right)^2 \left(\frac{T_e}{10^4 \text{K}} \right)^{-0.45} \times \left(\frac{\nu}{\text{GHz}} \right)^{0.1} \quad (1)$$

where S_ν (in Jy) is the total flux density of the H II region, D is the distance in kpc, T_e is the electron temperature, and ν is the frequency in GHz. With the help of the equation 1, $T_e = 10^4$ K, and $D = [1.4 \text{ kpc}$,

2.4 kpc; see Section 3.1.2 for more details], we determine $\log N_{\text{UV}}$ of each ionized clump marked in Figure 1a. Using the reference of Panagia (1973), these clumps (i.e., A–I) are found to be powered by massive B0.5V–O9.5V type stars. Furthermore, following the equations and analysis adopted in Dewangan et al. (2017a), the typical value of the initial particle number density of the ambient neutral gas ($n_0 = 10^3$ (10^4) cm^{-3}) leads a range of dynamical age of the ionized clumps (i.e., A–I) to be ~ 0.1 – 0.3 (0.3 – 1) Myr. The analysis shows the presence of massive stars in both the ionized filaments, which are distributed along the filaments.

3.1.2 Distribution of dust clumps, protostars, and molecular gas toward ionized filaments

In this section, we explore the multi-wavelength data sets to examine the embedded dust/molecular structures and protostars/young stellar objects (YSOs) against the ionized features around $l = 345^\circ.5$.

Figure 2a shows a 3-color composite map made using the *Herschel* 160 μm (in red), *Herschel* 70 μm (in green), and WISE 12 μm (in blue) images. Filamentary structures and bubble-like features are clearly visible in the infrared images, which trace the dust emission. The inset on the top right presents an area – hosting i17008, i17009, and S11 – in the zoomed-in view using the *Herschel* 160 μm image, showing the earlier reported one HFS toward i17008 and i17009. The inset on the bottom left displays an area hosting IRAS 17028–4050 in the zoomed-in view using the *Herschel* 160 μm image, showing the infrared bubble-like features.

We have examined the Mopra $^{13}\text{CO}(J = 1-0)$ emission in a velocity range of $[-21, -10]$ km s^{-1} to study the distribution of molecular gas. Figure 2b displays the Mopra $^{13}\text{CO}(J = 1-0)$ integrated emission map (moment-0) overlaid with the positions of the ATLASGAL clumps at 870 μm (see circles and stars). Note that Urquhart et al. (2018) also determined the reliable velocities and distances of the ATLASGAL clumps, which can be used to study the physical connection of different sub-regions in a given large area. In Figure 2b, the ATLASGAL clumps marked by stars and circles are located at a distance of 2.4 kpc and 1.4 kpc, respectively (see Urquhart et al. 2018, for more details). The ATLASGAL clumps associated with the ^{13}CO outflows are highlighted by plus symbols (in cyan; see Figure 2b). This information is taken from Yang et al. (2022), who listed the detection of the ^{13}CO outflows. They also provided the velocity ranges of the $^{13}\text{CO}(J = 2-1)$ red and blue wing-like velocity components toward the ATLASGAL clumps associated with outflows using the SEDIGISM $^{13}\text{CO}(J = 2-1)$ and $\text{C}^{18}\text{O}(J = 2-1)$ line data. All filled symbols show the clumps with V_{lsr} of $[-24, -8]$ km s^{-1} . On the other hand, open circles and stars represent clumps with V_{lsr} of $[-7, 0]$ km s^{-1} and $[-30, -25]$ km s^{-1} , which may not be associated with IF-A and IF-B. Note that in the direction of both the ionized filaments IF-A and IF-B, the Mopra molecular gas is depicted in the same velocity range of $[-21, -10]$ km s^{-1} . On the basis of the distances to the ATLASGAL clumps, IF-A and IF-B appear to be located at a distance of 2.4 kpc and 1.4 kpc, respectively.

In Figure 2c, the distribution of ionized emission (red contours) and the positions of 26 IRAS sources (filled pentagons) are presented against the molecular emission. The distribution of molecular gas traces a continuous structure toward IF-A, but a deficiency of molecular gas is seen toward the central part of IF-B (see Figure 2c). At least one molecular condensation is found toward both the ends of IF-B. From Figure 2a, we infer a continuous structure in the infrared images toward IF-B. Based on multi-wavelength images and distribution of the ATLASGAL clumps, we suggest that

there was an elongated molecular filament (see a dotted curve in Figure 2c), which has been eroded by the impact of massive stars located at the center of IF-B.

We examined the *Spitzer*-GLIMPSE photometric data at 3.6–5.8 μm , which allowed us to identify younger protostars (i.e., Class I YSOs) in our selected target area. The photometric magnitudes of point-like sources at *Spitzer* 3.6–5.8 μm bands were collected from the GLIMPSE-I Spring’ 07 highly reliable catalog (Benjamin et al. 2003). Class I YSOs are selected using the infrared color conditions (i.e., $[4.5] - [5.8] \geq 0.7$ mag and $[3.6] - [4.5] \geq 0.7$ mag) described in Hartmann et al. (2005) and Getman et al. (2007). In Figure 2d, we display the positions of Class I YSOs overlaid on the Mopra ^{13}CO map. An elongated filament traced in the 870 μm continuum map (see Dewangan et al. 2018c) and the location of the bubble S11 are also indicated by a curve and a big circle (average radius = 2.43 or 1.7 pc at a distance of 2.4 kpc), respectively.

In this work, we focus on only those Class I YSOs, which are distributed toward the clumpy structures in the clouds (see filled squares in Figure 2d). Such selection is considered by the visual inspection of the molecular gas and dust emissions (see the *Herschel* 160 μm emission in Figure 2a and the ATLASGAL clumps in Figure 2b). Several Class I YSOs appear to be located outside the molecular cloud boundary, which is traced using the Mopra ^{13}CO emission contour with a level of 4.3 K km s^{-1} (see Figure 2d). Hence, such Class I YSOs are unlikely to be part of the target clouds (see open squares in Figure 2d). Therefore, we have not made any attempt to study the Class I YSOs, which are highlighted by open squares in Figure 2d. In order to get distance information of the selected protostars (see filled squares in Figure 2d), we examined point-like sources in the Gaia EDR3 catalog (Gaia Collaboration et al. 2021; Bailer-Jones et al. 2021).

In the direction of the clouds traced in Figure 2c, the distance distribution of Gaia point-like sources peaks around a distance of 2.5 kpc (not shown here). It is expected that the optical counterparts of the selected Class I YSOs may be faint and/or may not be detected in the Gaia EDR3 catalog. We find optical counterparts of some Class I YSOs toward the clouds. The distances of some of these sources are in agreement with the dust clumps. In this relation, we have displayed the GAIA optical counterparts of Class I YSOs by cyan filled squares ($d = [1.6, 1.96]$ kpc) and green filled squares ($d = [2.0, 2.6]$ kpc) in Figure 2d. This particular analysis favors that the Class I YSOs spatially seen toward the clumpy structures in the clouds are likely to be physically connected with the ionized emission, dust clumps and molecular material. Hence in other words, in the direction of IF-A, we find an obvious correspondence among the ionized emission, dust clumps and molecular material, where Class I YSOs are distributed. From Figures 2b and 2d, dust clumps and Class I YSOs are also seen toward the central part of IF-B, where a deficiency of molecular gas is found.

In general, an average age of Class I YSOs is reported to be ~ 0.44 Myr (Evans et al. 2009). Overall, the early phases of star formation activities and the presence of massive stars are evident toward the parent clouds of the ionized filaments (see Figure 2d).

3.2 SEDIGISM $^{13}\text{CO}(J = 2-1)$ and $\text{C}^{18}\text{O}(J = 2-1)$ emission

In this section, we study the kinematics of molecular gas around $l = 345^\circ.5$, allowing us to examine gas velocity structures. Such knowledge is essential to probe the ongoing physical processes toward the selected target area.

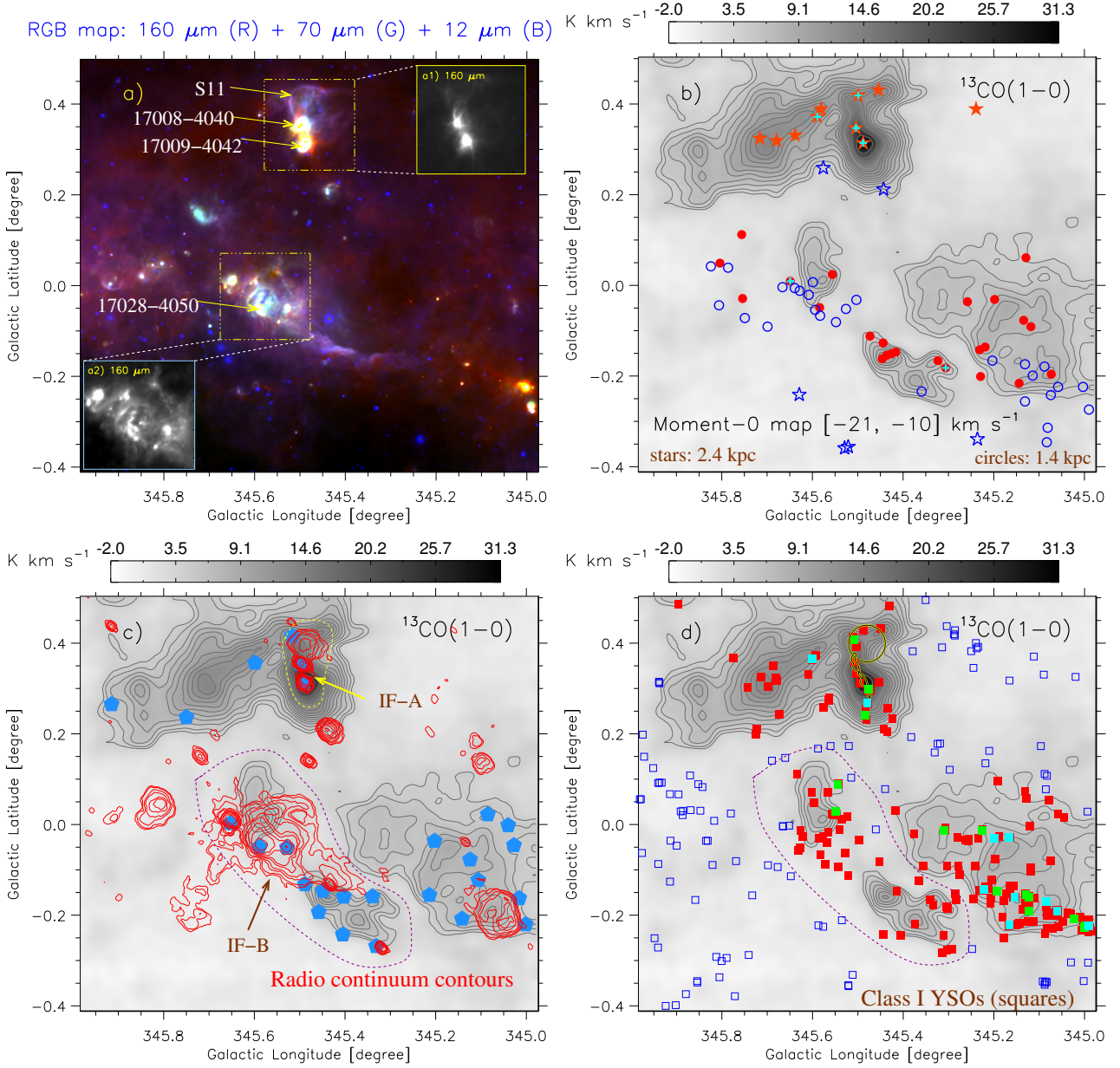


Figure 2. a) The panel shows a 3-color composite map made using the *Herschel* 160 μm (in red), *Herschel* 70 μm (in green), and WISE 12 μm (in blue) images. Using the *Herschel* 160 μm image, a zoomed-in view around i17008 is shown in the inset on the top right, while a zoomed-in view around IRAS 17028-4050 is presented in the inset on the bottom left. b) The panel presents the Mopra $^{13}\text{CO}(J=1-0)$ integrated intensity emission map at $[-21, -10]$ km s^{-1} . The Mopra ^{13}CO emission contours are also plotted with the levels of 4.3, 5, 6, 7, 8, 9, 10, 11, 12, 13, 16, 20, and 25 K km s^{-1} . The Mopra ^{13}CO line intensity is presented in terms of the antenna temperature. The molecular map is also overlaid with the positions of ATLASGAL clumps at 870 μm (see stars and circles; from [Urquhart et al. 2018](#)). All circles show the ATLASGAL clumps located at $d = 1.4$ kpc, while stars represent the ATLASGAL clumps situated at $d = 2.4$ kpc. All the filled symbols show the ATLASGAL clumps with V_{lsr} of $[-24, -8]$ km s^{-1} , while all the open symbols highlight the ATLASGAL clumps with V_{lsr} of $[-7, 0]$ km s^{-1} and $[-30, -25]$ km s^{-1} . Plus symbols show the ATLASGAL clumps associated with the ^{13}CO outflows (see [Yang et al. 2022](#), for more details). c) Overlay of the SUMSS 843 MHz radio continuum contours (in red; see Figure 1a) on the Mopra ^{13}CO intensity emission map. Filled pentagons represent the positions of 26 IRAS sources located in the direction of elongated morphologies. Arrows indicate two ionized filaments (IF-A and IF-B) in the panel. d) Overlay of Class I YSOs (see filled and open squares) on the Mopra ^{13}CO intensity emission map. This paper mainly focuses on the Class I YSOs, which are indicated by filled squares. Gaia optical counterparts of some selected Class I YSOs are available, and are highlighted by cyan filled squares ($d = [1.6, 1.96]$ kpc) and green filled squares ($d = [2.0, 2.6]$ kpc). An elongated filament and the bubble S11 are highlighted by a solid curve and a big circle, respectively. The elongated filament hosts the sites i17008 and i17009, and was traced using the 870 μm continuum map (see [Dewangan et al. 2018c](#)). In panels “c” and “d”, the Mopra molecular emission contours are also shown as presented in Figure 2b, and the extent of the elongated cloud hosting IF-B is indicated by a dotted curve (in magenta).

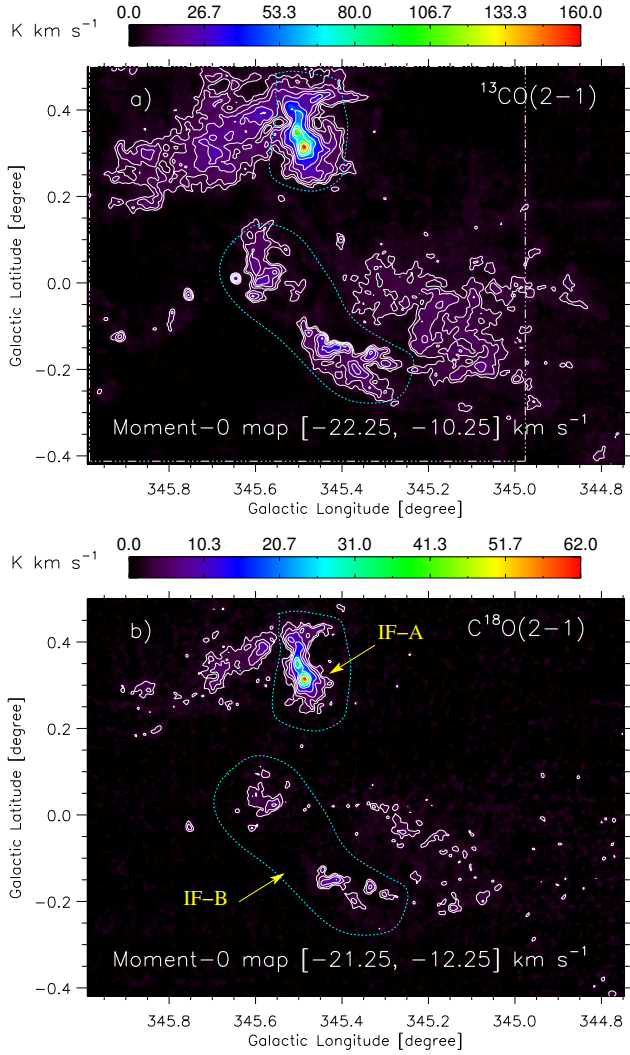


Figure 3. a) SEDIGISM $^{13}\text{CO}(J=2-1)$ map of intensity (moment-0) in the direction of our selected target area (see Figure 1a). The molecular emission is integrated from -22.25 to -10.25 km s^{-1} . The ^{13}CO emission contours are also shown with the levels of 7, 10, 15, 20, 28, 48, 70, 90, and 120 K km s^{-1} . A dotted-dashed box highlights an area covered by Mopra line data (see Figure 2b). b) SEDIGISM $\text{C}^{18}\text{O}(J=2-1)$ moment-0 map. The molecular emission is integrated from -21.25 to -12.25 km s^{-1} . The C^{18}O emission contours are also shown with the levels of 2.6, 4.3, 7, 11, 20, 28, and 42 K km s^{-1} . In each panel, dotted curves indicate the elongated parent clouds of IF-A and IF-B.

3.2.1 Molecular clouds hosting IF-A and IF-B

Here we study the spatial and velocity distribution of the SEDIGISM $^{13}\text{CO}(J=2-1)$ and $\text{C}^{18}\text{O}(J=2-1)$ emission in the area shown in Figure 1a. Figures 3a and 3b present the $^{13}\text{CO}(J=2-1)$ and $\text{C}^{18}\text{O}(J=2-1)$ integrated maps and contours, respectively, where enclosed regions indicate the areas around the ionized filaments. The integrated intensity or moment-0 maps of $^{13}\text{CO}(J=2-1)$ and $\text{C}^{18}\text{O}(J=2-1)$ are produced using velocity intervals of $[-22.25, -10.25]$ and $[-21.25, -12.25]$ km s^{-1} , respectively. Similar morphologies of clouds are evident in the Mopra $^{13}\text{CO}(J=1-0)$ and the SEDIGISM $^{13}\text{CO}(J=2-1)$ maps. However, one can keep in mind that the SEDIGISM molecular maps (beam size $\sim 41''$) provide more insight into the clouds due to its relatively better resolution compared to the Mo-

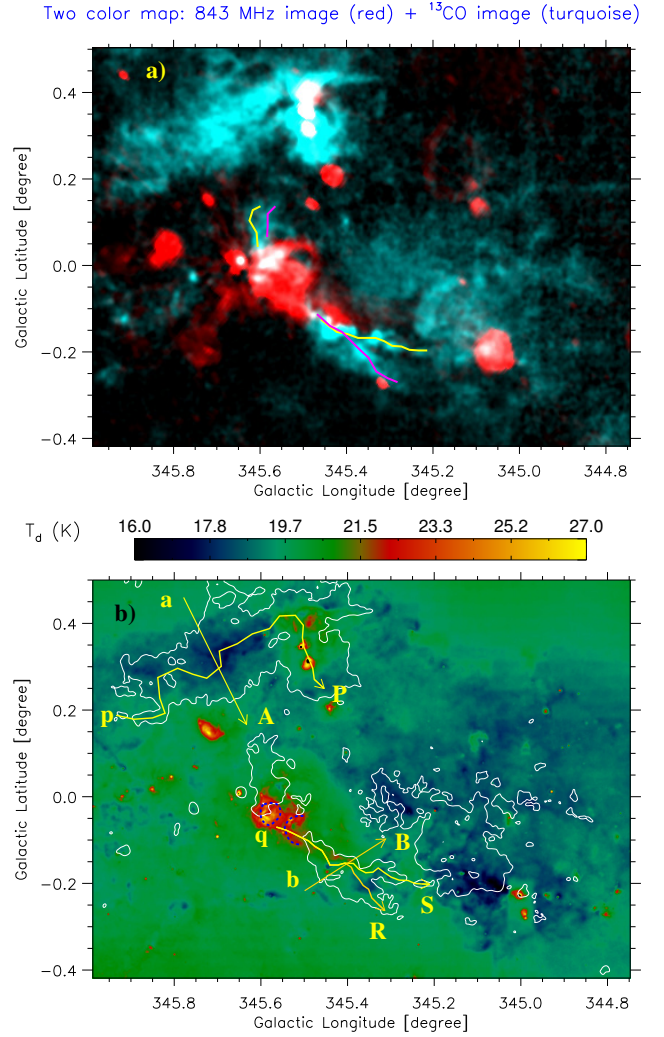


Figure 4. a) The panel shows a two-color composite image made using the SUMSS 843 MHz continuum emission (in red) and the $^{13}\text{CO}(J=2-1)$ moment-0 map (in turquoise color; see Figure 3a). In the direction of IF-B, at least two elongated molecular filaments are indicated by curves. b) The panel displays the overlay of the $^{13}\text{CO}(J=2-1)$ emission contour (see Figure 3a) on the *Herschel* temperature map. Two arrows (i.e., aA and bB) and three curves (i.e., pP, qR and qS) are indicated in the panel, where the position-velocity diagrams are produced (see Figures 5e, 5f, and 6). Blue dashed curves highlight bubble-like structures in the temperature map.

pra line data (beam size $\sim 96''$). In Figure 3b, the $\text{C}^{18}\text{O}(J=2-1)$ emission enables us to depict denser parts in the molecular clouds as traced by the $^{13}\text{CO}(J=2-1)$ emission (see areas of enclosed regions in Figures 3a and 3b).

In Figure 4a, we display a two-color composite map made using the SUMSS 843 MHz continuum map (in red) and the SEDIGISM $^{13}\text{CO}(J=2-1)$ map (in turquoise). IF-A is embedded in the filamentary molecular cloud, which is distinctly traced in the $\text{C}^{18}\text{O}(J=2-1)$ map (see Figure 3b). The color composite map indicates the destruction of the central part of an elongated molecular (i.e., $^{13}\text{CO}(J=2-1)$ and $\text{C}^{18}\text{O}(J=2-1)$) structure, where IF-B is spatially traced. The color composite map also hints at the presence of two filamentary molecular clouds toward IF-B, which are indicated by two curves in Figure 4a. Figure 4b displays the *Herschel* temperature

map overlaid with the SEDIGISM $^{13}\text{CO}(J = 2-1)$ emission contour. The areas around i17008 and i17009 are saturated in the *Herschel* temperature map. Warm dust emission ($T_d > 21$ K) is evident toward both the ionized filaments. In the direction of the ionized clumps “E” and “F” in IF-B (see Figure 1a), at least two bubble-like structures are observed in the *Herschel* temperature map (see blue dashed curves in Figure 4b), where the molecular gas depression is found.

Figures 5a and 5b present the line velocity/velocity field/moment-1 map of the SEDIGISM $^{13}\text{CO}(J = 2-1)$ and $\text{C}^{18}\text{O}(J = 2-1)$ emission, respectively. Both these moment-1 maps indicate a noticeable velocity spread toward the clouds associated with both the ionized filaments, where higher values of line widths (> 1.5 km s $^{-1}$) are found in the intensity-weighted line width maps (moment-2) of $^{13}\text{CO}(J = 2-1)$ and $\text{C}^{18}\text{O}(J = 2-1)$ (see Figures 5c and 5d).

Position-velocity diagrams of the $^{13}\text{CO}(J = 2-1)$ emission along arrows “aA” and “bB” (see Figure 4b) are presented in Figures 5e and 5f, respectively. The contours of the $\text{C}^{18}\text{O}(J = 2-1)$ emission are also drawn in both the position-velocity diagrams. Along the direction of the arrow “aA”, the position-velocity diagram hints the existence of two velocity peaks/components around -11 and -17 km s $^{-1}$ (see arrows in Figure 5e). Note that the arrow “bB” passes through the overlapping areas of two filamentary molecular clouds in the direction of IF-B. Along the arrow “bB”, we find at least two velocity peaks/components around -16 and -19 km s $^{-1}$, exhibiting the presence of two distinct filaments (see arrows in Figure 5f). Figures 6a, 6b, and 6c display position-velocity diagrams of the $^{13}\text{CO}(J = 2-1)$ emission along curves “pP”, “qR” and “qS”, which are marked in Figure 4b. In the direction of i17008, an outflow (blue wing: $(-25.2, -19.8)$ km s $^{-1}$; red wing: $(-14.8, -6.2)$ km s $^{-1}$; Yang et al. 2022) is evident. We can also trace an outflow (blue wing: $(-22.8, -20.5)$ km s $^{-1}$; red wing: $(-13.5, -9.8)$ km s $^{-1}$; Yang et al. 2022) toward i17009. Apart from the outflow activity, in the direction of i17009, two velocity components (around -15 and -18 km s $^{-1}$) are also seen (see arrows in Figure 6a). Furthermore, two distinct velocity peaks (around -15 and -18 km s $^{-1}$) are also evident along the curves “qR” and “qS” (see arrows in Figures 6b and 6c).

3.2.2 Zoomed-in view of molecular cloud associated with IF-A

In the direction of an area hosting i17008, i17009, and S11 (or ionized clumps “A–C”), Figures 7a, 7b, and 7c display the moment-0, moment-1, and moment-2 maps of $^{13}\text{CO}(J = 2-1)$, respectively. In Figures 7d, 7e, and 7f, we show moment-0, moment-1, and moment-2 maps of $\text{C}^{18}\text{O}(J = 2-1)$, respectively. The $^{13}\text{CO}(J = 2-1)$ emission is integrated over a velocity range of $[-24, -9]$ km s $^{-1}$ (see Figure 7a), while the $\text{C}^{18}\text{O}(J = 2-1)$ emission is integrated over a velocity range from -22 to -12 km s $^{-1}$ (see Figure 7d). A dotted circle in each panel of Figure 7 highlights the location of the bubble S11. The moment-0 maps of $^{13}\text{CO}(J = 2-1)$ and $\text{C}^{18}\text{O}(J = 2-1)$ show the elongated filamentary structure (see Figures 7a and 7d), which has almost a similar morphology as seen in the ATLASGAL continuum map at $870\ \mu\text{m}$ (see Figure 2d). However, the proposed HFSs are not very clearly seen in both the moment-0 maps.

The moment-1 maps of $^{13}\text{CO}(J = 2-1)$ and $\text{C}^{18}\text{O}(J = 2-1)$ show a noticeable velocity difference/gradient toward the northern direction compared to the site i17009. In the direction of both the IRAS sites, we find higher values of line width (> 2.5 km s $^{-1}$) (see Figures 7c and 7f). One can also find higher line width (i.e., $1-2.5$ km s $^{-1}$) toward the bubble in the moment-2 maps of $^{13}\text{CO}(J = 2-1)$ and $\text{C}^{18}\text{O}(J = 2-1)$. The increased line widths can suggest

star formation activities and/or the presence of multiple velocity components.

Figure 8 shows the averaged spectra of $^{13}\text{CO}(J = 2-1)$ and $\text{C}^{18}\text{O}(J = 2-1)$ over eight small circles (radius = $20''$) distributed toward the elongated molecular cloud (see Figure 7f). For a reference purpose, a vertical dashed line at $V_{\text{lsr}} = -18$ km s $^{-1}$ is also marked in each panel of Figure 8. The circle nos. #1–3 are distributed toward the bubble, while the circle nos. #4 and #6 are located toward the sites i17008 and i17009, respectively. The spectra of $^{13}\text{CO}(J = 2-1)$ and $\text{C}^{18}\text{O}(J = 2-1)$ show a single velocity peak toward four positions (#3, 4, 5, and 8). However, we may see at least two velocity peaks in the direction of the other four positions (#1, 2, 6, and 7). In particular, based on the $^{13}\text{CO}(J = 2-1)$ and $\text{C}^{18}\text{O}(J = 2-1)$ spectra toward the circle #6, two velocity peaks are clearly found, allowing us to identify two cloud components at $[-15.25, -11]$ km s $^{-1}$ (around -15 km s $^{-1}$) and $[-22.25, -16]$ km s $^{-1}$ (around -18 km s $^{-1}$). Furthermore, with respect to the reference line, we find a change in the velocity peaks of molecular spectra on moving from the northern to southern parts of the cloud, showing the existence of a velocity gradient in the molecular cloud.

Figures 9 and 10 display the integrated velocity channel contours of $^{13}\text{CO}(J = 2-1)$ and $\text{C}^{18}\text{O}(J = 2-1)$ (at velocity intervals of 1 km s $^{-1}$), respectively. Both channel maps support the presence of two molecular cloud components toward the area hosting two IRAS sources and the bubble (see panels at $[-19, -18]$ and $[-16, -15]$ km s $^{-1}$). The channel maps also support the presence of the HFS toward each IRAS site (see panels between $[-22, -21]$ and $[-17, -16]$ km s $^{-1}$).

Figures 11a and 11b show the position-velocity diagrams of $^{13}\text{CO}(J = 2-1)$ and $\text{C}^{18}\text{O}(J = 2-1)$ along the curve as marked in Figures 7a and 7d, respectively. In Figures 11c and 11d, we present the latitude-velocity diagrams of $^{13}\text{CO}(J = 2-1)$ and $\text{C}^{18}\text{O}(J = 2-1)$ for a longitude range of $345^\circ.43$ to $345^\circ.54$. A continuous velocity structure is seen in all the position-velocity diagrams. These maps also suggest the presence of an outflow toward i17008 and the presence of two velocity components (around -15 and -18 km s $^{-1}$). All these results together favour the spatial and velocity connections of two cloud components in the direction of i17008, i17009, and S11.

Figures 12a and 12b present the overlay of the $^{13}\text{CO}(J = 2-1)$ and $\text{C}^{18}\text{O}(J = 2-1)$ emission contours of two cloud components (at $[-15.25, -11]$ and $[-22.25, -16]$ km s $^{-1}$) on the *Spitzer* $8.0\ \mu\text{m}$ image, respectively. The location of the elongated filament is also indicated in Figures 12a and 12b. In the *Spitzer* $8.0\ \mu\text{m}$ image, the extended emissions detected toward both the IRAS sites and the bubble (or ionized clumps “A–C”) are seen toward the overlapping areas of two clouds.

On the basis of the channel maps, we produce an integrated emission map of $^{13}\text{CO}(J = 2-1)$ at $[-17.75, -16.5]$ km s $^{-1}$ to trace the proposed HFSs (see Figure 12c). In this relation, we exposed this $^{13}\text{CO}(J = 2-1)$ map to an edge detection algorithm (i.e. Difference of Gaussian (DoG); see Gonzalez & Woods 2002; Assirati et al. 2014; Dewangan et al. 2017b). In Figure 12d, we display a two-color composite map made using the $^{13}\text{CO}(J = 2-1)$ maps, which consists of the “Edge-DoG” processed $^{13}\text{CO}(J = 2-1)$ map at $[-17.75, -16.5]$ km s $^{-1}$ (in red) and the $^{13}\text{CO}(J = 2-1)$ map at $[-24, -9]$ km s $^{-1}$ (in turquoise). In Figure 12d, at least five curves are marked and labeled in the direction of i17008 (or ionized clump “B”), while at least three curves are highlighted toward i17009 (or ionized clump “C”). In Figure 12d, one can clearly see the HFS toward each IRAS site.

In Figure 12e, we present the integrated emission map

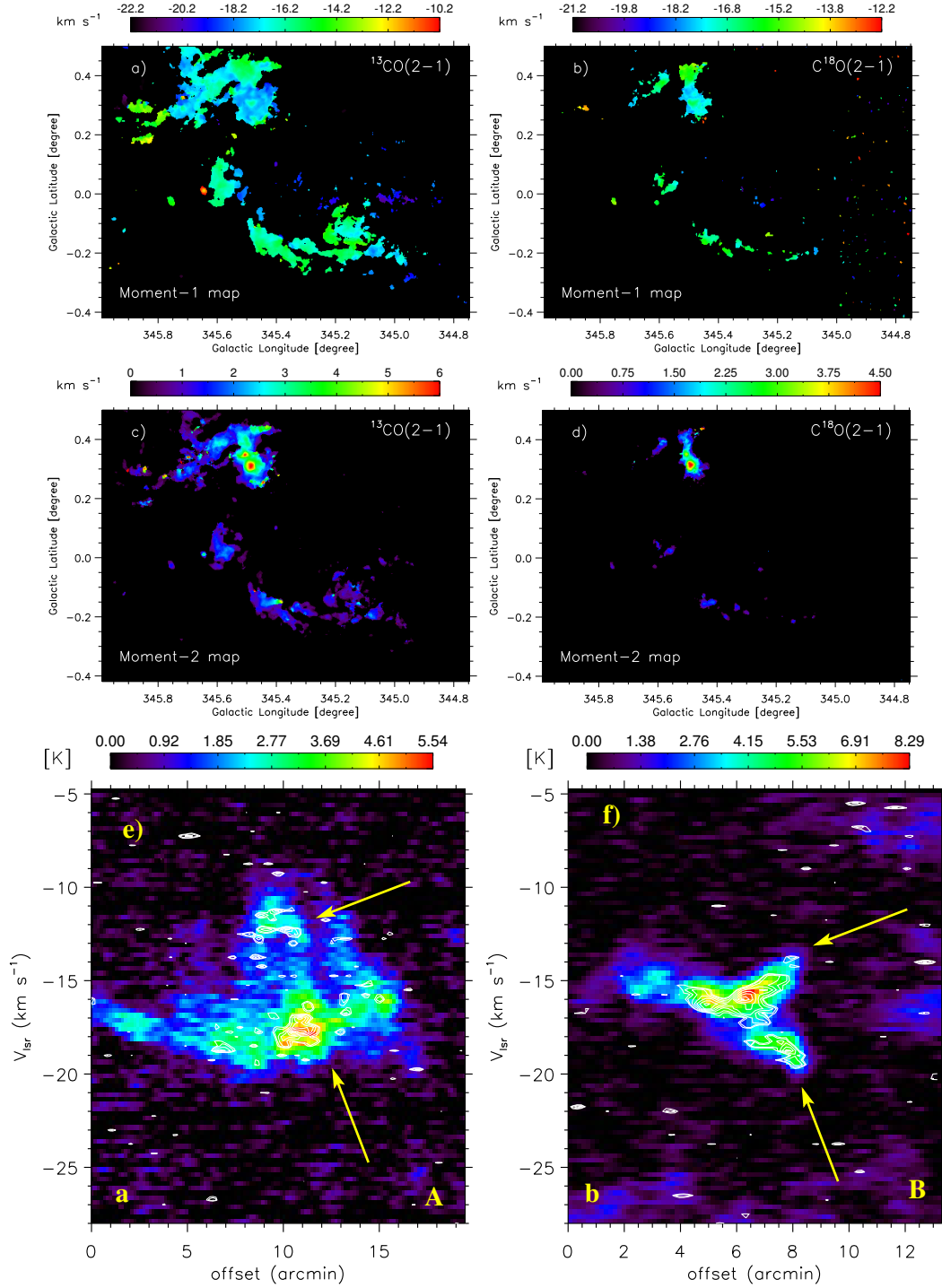


Figure 5. a) $^{13}\text{CO}(J=2-1)$ moment-1 map of our selected target area (see a dotted-dashed box in Figure 1a). b) $\text{C}^{18}\text{O}(J=2-1)$ moment-1 map. c) $^{13}\text{CO}(J=2-1)$ moment-2 map. d) $\text{C}^{18}\text{O}(J=2-1)$ moment-2 map. e) Position-velocity diagram of $^{13}\text{CO}(J=2-1)$ along the arrow “aA” (see Figure 4b). White contours are the $\text{C}^{18}\text{O}(J=2-1)$ emission. The levels of the $\text{C}^{18}\text{O}(J=2-1)$ emission contours are $(0.35, 0.4, 0.5, 0.6, 0.7, 0.8, 0.9, 0.98) \times 2.37$ K. f) Position-velocity diagram of $^{13}\text{CO}(J=2-1)$ along the arrow “bB” (see Figure 4b). White contours are the $\text{C}^{18}\text{O}(J=2-1)$ emission. The levels of the $\text{C}^{18}\text{O}(J=2-1)$ emission contours are $(0.35, 0.4, 0.5, 0.6, 0.7, 0.8, 0.9, 0.98) \times 2.23$ K. In panels “e” and “f”, arrows indicate structures with different velocities.

(moment-0) at $[-21, -14]$ km s $^{-1}$ of the dense gas tracer $\text{N}_2\text{H}^+(1-0)$ from the MALT90 data sets, which were observed for the areas covering G345.504/i17008 and G345.487/i17009 (see dotted-dashed boxes in Figure 12c). Note that the MALT90 line data sets are not available toward the bubble S11. The location of the elongated filament is also highlighted in the moment-0 map. The moment-0 map

of N_2H^+ clearly displays the filamentary morphology as seen in the ATLASGAL continuum map at $870 \mu\text{m}$.

Figure 12f displays the position-velocity diagram of N_2H^+ data set along the axis as marked in the N_2H^+ map (see Figure 12e). In the position-velocity diagram of the N_2H^+ line, the hyperfine components are also evident. The position-velocity diagram supports

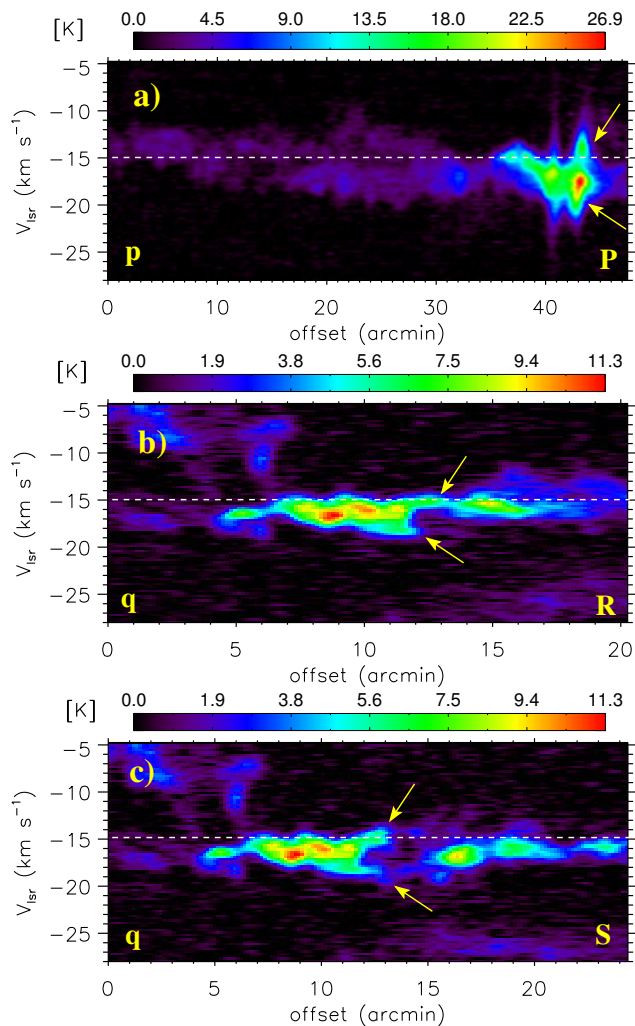


Figure 6. Position-velocity diagrams of $^{13}\text{CO}(J = 2-1)$ along the curves a) “pP”; b) “qR”; c) “qS” (see Figure 4b). Arrows indicate structures with different velocities.

the existence of a continuous velocity structure along the selected axis or filament hosting G345.504/i17008 and G345.487/i17009, and also shows a velocity spread toward the site i17009.

The implication of all these observed findings is presented in Section 4.

4 DISCUSSION

In the direction of our selected target field around $l = 345^\circ.5$, this paper mainly focuses on the elongated filamentary structures traced in different emissions (i.e., dust, molecular, and ionized). One of the new findings of this work is the presence of two distinct ionized filaments (i.e., IF-A and IF-B) located at different distances (see Section 3.1.2). Interestingly, the parent molecular clouds of both the ionized filaments are depicted in the same velocity range of $[-21, -10] \text{ km s}^{-1}$, and have filamentary appearances. Several ionized clumps, which are excited by massive stars, are depicted toward the ionized filaments (see Figure 1 and Section 3.1.1). In the following sections, we discuss the origin of massive stars and elongated ionized structures.

4.1 Interacting filamentary molecular clouds

We investigate at least two cloud components toward the parent molecular clouds of both the ionized filaments (see Section 3.2). It is another new finding of this work. In the direction of each parent molecular cloud, we find a velocity connection of two cloud components having a velocity separation of about 3 km s^{-1} (see Figure 6). These filamentary clouds also spatially overlap with each other along the major axis, backing the existence of their multiple common zones. It may be considered as one of the forms of molecular/dust filamentary twisting/coupling (e.g., LBN 140.07+01.64; Dewangan et al. 2021). This argument is valid for both the parent molecular clouds of IF-A and IF-B. These results together hint at the onset of the interaction or collision of filamentary molecular clouds, but do not favour a single point collision event of two molecular clouds. In the direction of the converging areas of the clouds, we find either dust clumps hosting massive stars or only ionized clumps powered by massive stars.

Earlier, signatures of the colliding flows were reported to Lupus I (Gaczowski et al. 2015, 2017; Krause et al. 2018). Lupus I is associated with the Lupus clouds, which are nearby (150-200 pc) and young (1-2 Myr) star-forming region (e.g., Gaczowski et al. 2015). Lupus I is spatially seen between the Upper-Scorpius (USco) HI shell and the Upper Centaurus-Lupus (UCL) wind bubble (Gaczowski et al. 2015). In other words, Lupus I is thought to be situated along a filament at the converging area of these two bubbles, where the higher level of clumpiness is observed. In this context, Lupus I has been suggested to be strongly influenced by colliding flows/shocked flows, which are produced by the expanding USco HI shell and the UCL wind bubble (Gaczowski et al. 2015, 2017; Krause et al. 2018). These earlier works encourage us to explore the scenario of the colliding flows in our selected target area.

Numerical simulations of the cloud cloud collision (CCC) process show the presence of massive and dense clumps/cores at the junction of two molecular clouds or the shock-compressed interface layer (e.g., Habe & Ohta 1992; Anathpindika 2010; Inoue & Fukui 2013; Haworth et al. 2015a,b; Torii et al. 2017; Balfour et al. 2017; Bisbas et al. 2017, and references therein), which is a very suitable environment for the MSF. In other words, massive stars and clusters of YSOs can be formed inside the dense gas layer produced via the strong compression at the colliding interface. In this relation, several observational works have been reported in the literature (e.g., Torii et al. 2011, 2015, 2017; Fukui et al. 2014, 2018, 2021; Dhanya et al. 2021). Observationally, in the CCC process, one may expect a bridge feature in position-velocity diagrams, showing a connection of two clouds by an intermediate velocity and low intensity feature in velocity space (e.g., Haworth et al. 2015b; Dewangan & Ojha 2017; Dewangan et al. 2018a; Kohno et al. 2018; Priestley & Whitworth 2021). In addition, one may also expect a complementary distribution (i.e., a spatial match of “key/intensity-enhancement” and “cavity/keyhole/intensity-depression” features) in the collision event (e.g., Fukui et al. 2018; Dewangan et al. 2018b; Enokiya et al. 2021). However, we do not find any complementary distribution of two clouds in our target area.

Our results enable us to propose the applicability of the collision of two filamentary clouds in areas hosting IF-A and IF-B. Previously, in a massive-star forming region S237, a cluster of YSOs and a massive clump were found toward at the intersection of filamentary features, and the collision of these features was proposed to explain the observed cluster formation (Dewangan et al. 2017a). Dewangan et al. (2019a) also identified two closely spaced (in ve-

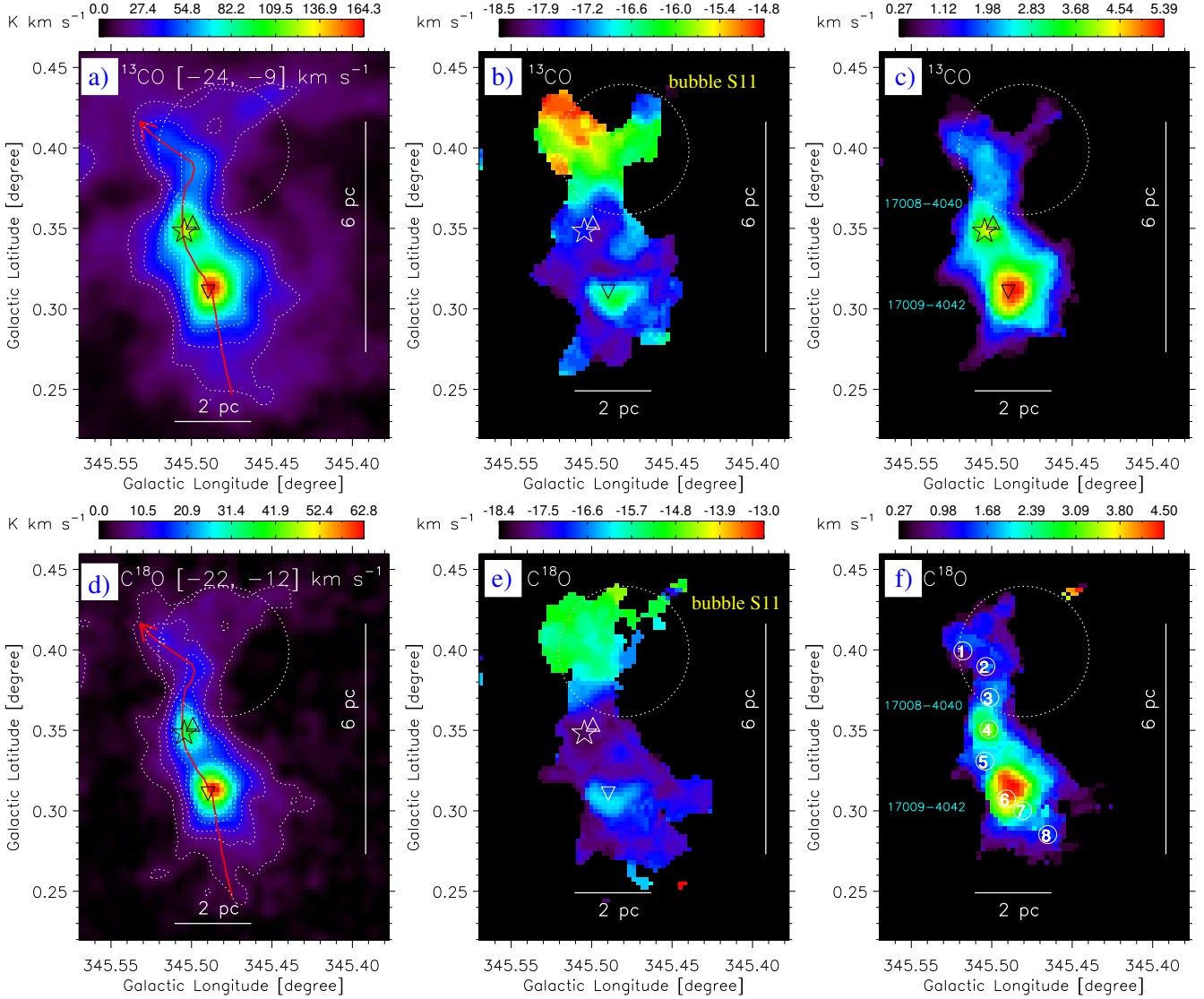


Figure 7. A zoomed-in view of an area around i17008 using molecular line data sets. a) $^{13}\text{CO}(J=2-1)$ map of intensity (moment-0). The molecular emission is integrated from -24 to -9 km s^{-1} . The ^{13}CO emission contours are also shown with the levels of $(0.13, 0.2, 0.3, 0.4) \times 164.3 \text{ K km s}^{-1}$. b) $^{13}\text{CO}(J=2-1)$ moment-1 map. c) $^{13}\text{CO}(J=2-1)$ moment-2 map. d) $\text{C}^{18}\text{O}(J=2-1)$ moment-0 map. The molecular emission is integrated from -22 to -12 km s^{-1} . The $\text{C}^{18}\text{O}(J=2-1)$ emission contours are also shown with the levels of $(0.06, 0.13, 0.2, 0.3, 0.4) \times 62.8 \text{ K km s}^{-1}$. e) $\text{C}^{18}\text{O}(J=2-1)$ moment-1 map. f) $\text{C}^{18}\text{O}(J=2-1)$ moment-2 map. Eight circles are marked and labeled, where averaged spectra are produced in Figure 8. In panels “a” and “d”, a curve (in red) is indicated, and position-velocity diagrams are extracted along it (see Figures 11a and 11b). In each panel, the positions of i17008, i17009, the MIR bubble S11, and 6.7 GHz MME are marked by triangle, upside down triangle, dotted circle, and star, respectively. In all panels, the scale bars derived at a distance of 2.4 kpc are shown.

locity as well as in position) filamentary clouds in star-forming site AFGL 5142 and deciphered the presence of young stellar clusters by the filamentary collision/interaction scenario. In the case of the AFGL 333-Ridge, Liang et al. (2021) traced two velocity components having a velocity separation of about 2.5 km s^{-1} . Based on the analysis of ^{13}CO line data, they proposed a scenario of colliding and merging of two cloud components into one molecular cloud in the AFGL 333-Ridge.

In the present study, we consider the spatial extent of the overlapping regions of the two clouds, having a velocity separation of $\sim 3 \text{ km s}^{-1}$, to be $\sim 1.75 \text{ pc}$. We estimate the collision time-scale (i.e., the time-scale for which the material is accumulated at the collision

zones) using the following equation (see also Henshaw et al. 2013)

$$t_{\text{accum}} = 2.0 \left(\frac{l_{\text{fcs}}}{0.5 \text{ pc}} \right) \left(\frac{v_{\text{rel}}}{5 \text{ km s}^{-1}} \right)^{-1} \left(\frac{n_{\text{pstc}}/n_{\text{prec}}}{10} \right) \text{ Myr} \quad (2)$$

where, n_{prec} and n_{pstc} are the mean densities of the pre-collision and post-collision region, respectively. Here, l_{fcs} is the collision length-scale and v_{rel} is the observed relative velocity. In the present case, we do not know the exact viewing angle of the collision. Therefore, a typical viewing angle of 45° results in the collision length-scale (l_{fcs}) of $\sim 2.5 \text{ pc}$ ($= 1.75 \text{ pc}/\sin(45^\circ)$), and the observed relative velocity (v_{rel}) of $\sim 4.2 \text{ km s}^{-1}$ ($= 3 \text{ km s}^{-1}/\cos(45^\circ)$). In this work, we do not have reliable estimates of n_{prec} and n_{pstc} values. However, logically, we expect $n_{\text{pstc}} > n_{\text{prec}}$ in a collision process, resulting in the higher mean density ratio (≥ 1) of the post- and pre-collision

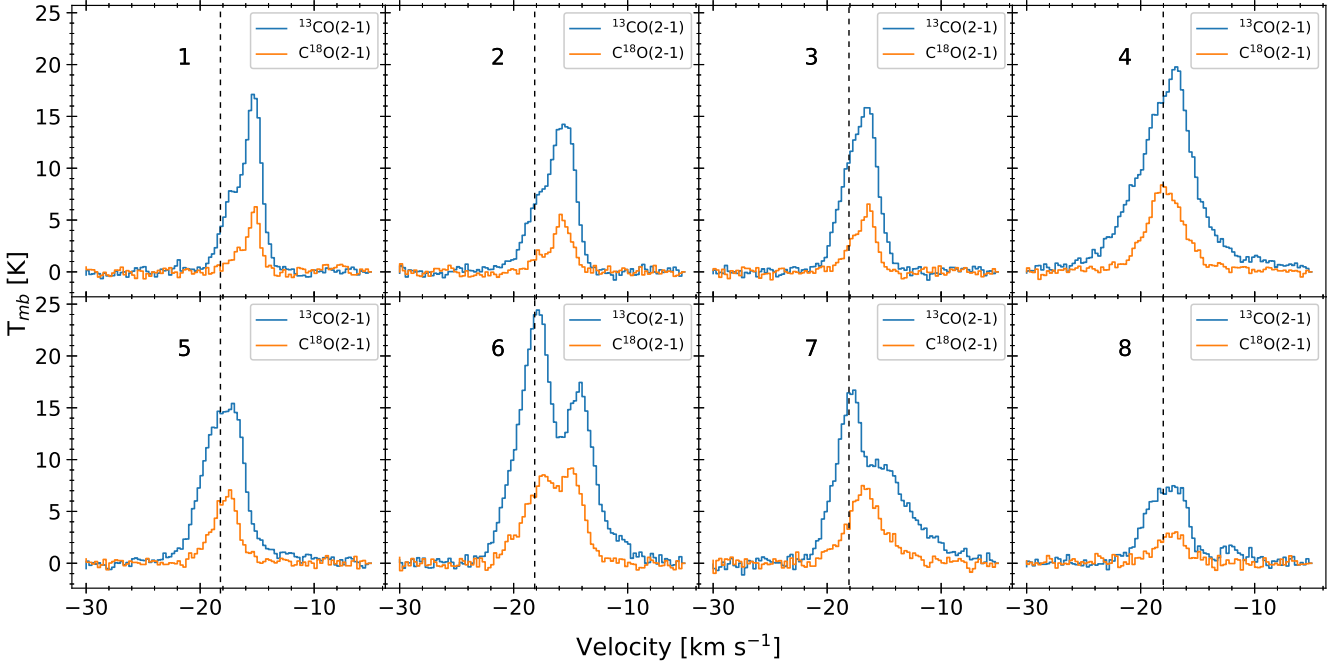


Figure 8. The $^{13}\text{CO}(J=2-1)$ (in blue) and $\text{C}^{18}\text{O}(J=2-1)$ (in orange) spectra toward eight areas as highlighted by circles in Figure 7f. A vertical line at $V_{\text{lsr}} = -18 \text{ km s}^{-1}$ is also indicated in each panel.

regions. Considering a wide range of the mean density ratio of 1–10, we compute a range of collision timescale of $\sim 1.2\text{--}11.7$ Myr. It implies that the collision of two clouds might have occurred ~ 1.2 Myr ago.

In Section 3.1.1, the dynamical ages of the ionized clumps (“A–G”) are computed to be $\sim 0.1\text{--}1$ Myr. In the direction of site i17008, an O-star candidate without an H II region has also been investigated. Also, the noticeable Class I protostars (mean age ~ 0.44 Myr) appear to be seen toward the parent clouds of IF-A and IF-B (see Figure 2d). Thus, considering different ages concerning signposts of star formation activities, we notice that the collision timescale is old enough to influence the star formation (including massive stars) in the parent molecular clouds of both the ionized filaments. Therefore, the star formation history in our target area seems to be explained by the collision of the two filamentary clouds.

The previously reported HFSs toward i17008 and i17009 are spatially seen in one of the cloud components (i.e., around -18 km s^{-1} ; see Figure 12). The presence of HFSs may favour the onset of the global non-isotropic collapse (GNIC) scenario (see Tigé et al. 2017; Motte et al. 2018, for more details). In the smoothed particle hydrodynamics simulations related to head-on collision of two clouds, Balfour et al. (2015) reported the presence of a pattern of filaments (e.g., hub or spokes systems) as resultant from the collision process. The theoretical work supports the origin of a shock-compressed layer by the colliding clouds, which fragments into filaments. Then these filaments form a network like a spider’s web in the case of higher relative velocity between clouds (see also magnetohydrodynamic (MHD) simulations of Inoue et al. (2018)). Recently, the review article on CCC of Fukui et al. (2021) also stated that the onset of the collision process can produce hub filaments with their complex morphology. Using the SEDIGISM ^{13}CO and C^{18}O line data, in the filamentary infrared dark cloud (IRDC) G333.73+0.37, Dewangan (2022) presented the results in favour of

CCC or converging flows, explaining the presence of the HFS and massive stars in the IRDC. Using the $\text{N}_2\text{H}^+(1-0)$ observations, Beltrán et al. (2022) explained the formation of the HFS and the origin of massive protocluster associated with the hot molecular core in the G31.41+0.31 cloud through the CCC. In the case of N159E-Papillon Nebula located in the Large Magellanic Cloud (distance ~ 50 kpc), Fukui et al. (2019) provided observational results to support the scenario of the large-scale colliding flow, which was used to explain the existence of massive stars and HFSs. These observational findings strongly support the connection of the formation of HFSs and massive stars with the CCC. Hence, our proposed collision process may also explain the existence of hubs in our target area.

Overall, the interaction of elongated molecular filaments seems to be responsible for the birth of massive stars associated with IF-A and IF-B.

4.2 Ionized filaments IF-A and IF-B

In recent years, a wealth of studies on dust and molecular filaments have been carried out in star-forming sites, which strongly support their key role in the formation of stellar clusters and massive stars. Despite the availability of numerous radio continuum surveys, so far a very limited number of studies have conducted to investigate elongated ionized structures with high aspect ratios (length/thickness) in massive star-forming regions (e.g., Lynds Bright Nebulae (Karr & Martin 2003), Eridanus filaments (Pon et al. 2014), Cygnus X (Emig et al. 2022)), which can be referred to as ionized filaments.

In general, the study of massive star-forming regions is largely focused on H II regions powered by massive OB stars, which are often surrounded by MIR bubbles having different morphologies (i.e., a complete or closed ring, a broken or incomplete ring, and a bipolar structure; Churchwell et al. 2006). In this context, one

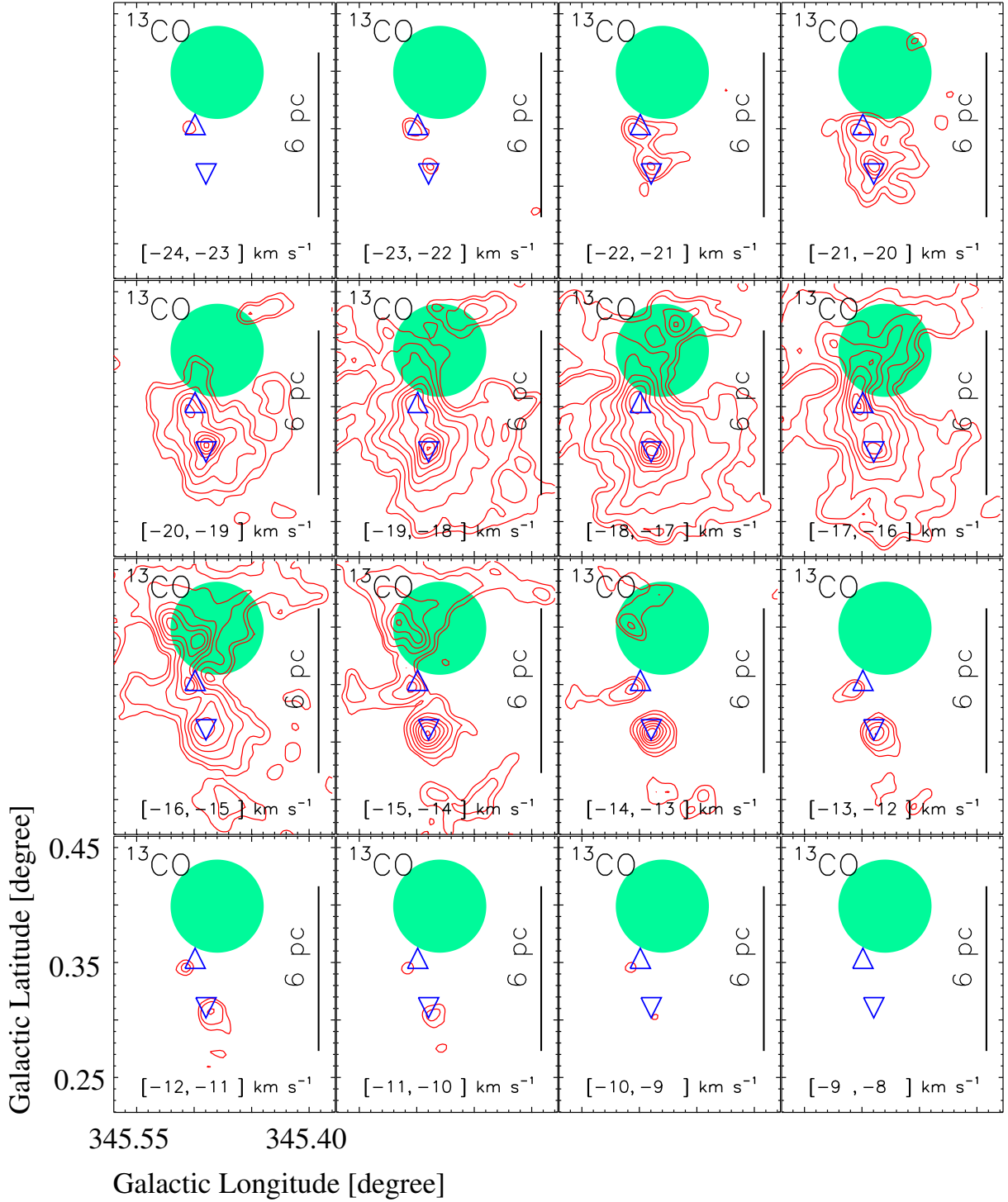


Figure 9. Integrated velocity channel contours (in red) of $^{13}\text{CO}(J=2-1)$ emission (at velocity intervals of 1 km s^{-1}) toward an area containing i17008 and i17009. The contour levels are 2.4, 3.5, 6, 9, 12, 15, 18, 21, 24, 27, and 30 K km s^{-1} . The scale bar and other symbols are the same as in Figure 7a. In each panel, a filled circle shows the location of the MIR bubble S11.

may not expect a very large elongated morphology of a single H II region excited by massive OB stars. In the literature, the ionized nature of the Lynds Bright Nebulae was explained by ultraviolet photons leaking from the nearby star-forming region W5 (Karr & Martin 2003). In the case of Eridanus filaments, Pon et al. (2014) reported that these filaments are non-equilibrium structures, and might have produced when the Orion-Eridanus superbubble com-

pressed a pre-existing gas cloud and swept up the gas into a dense ring around the outer boundary of the bubble. In the site Cygnus X, Emig et al. (2022) proposed that the energetic feedback from Cyg OB2 (i.e., ultraviolet (UV) radiation, stellar winds, and radiation pressure) may be responsible for the observed ionized filaments via swept-up ionized gas or dissipated turbulence. Hence, the common

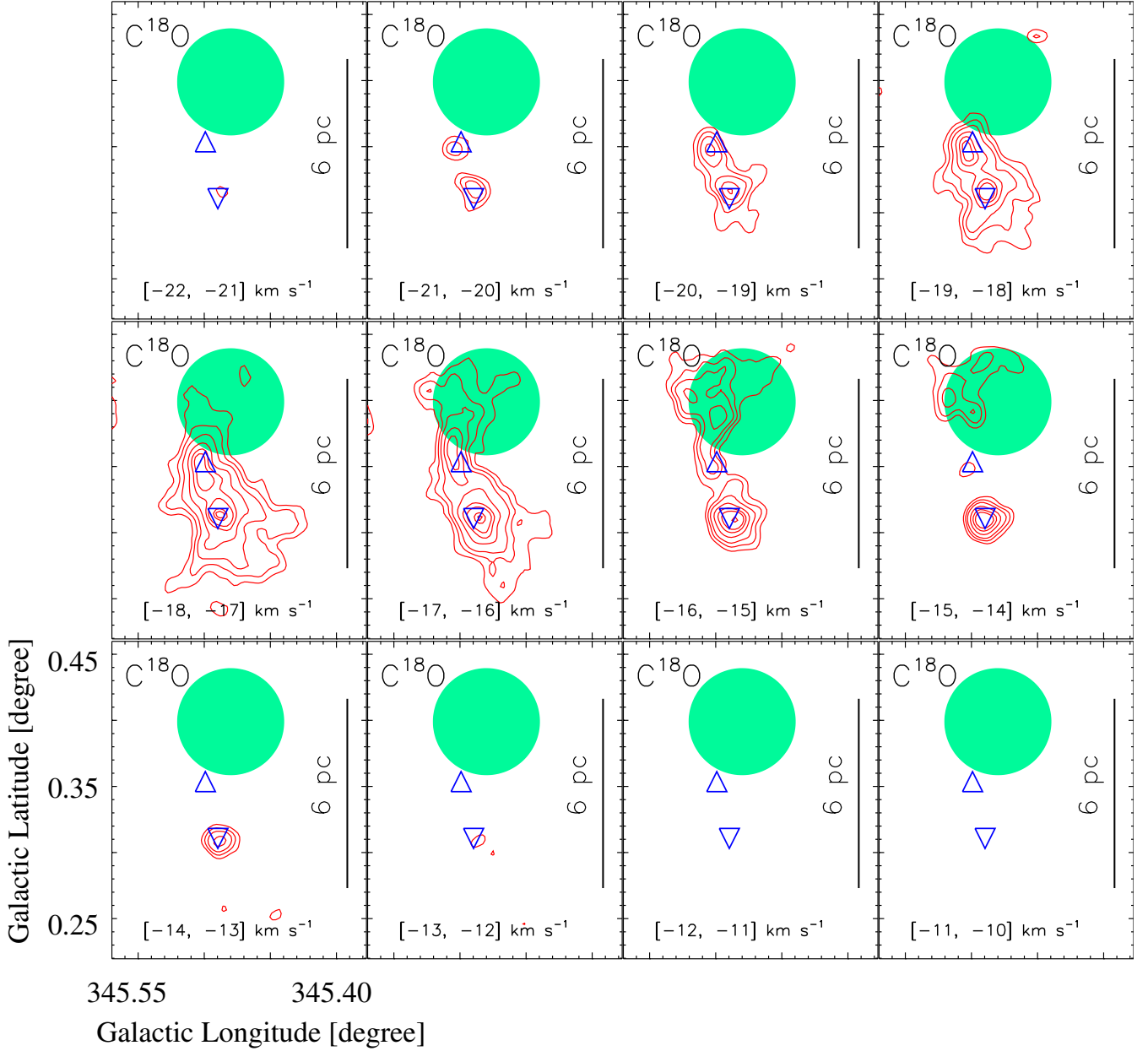


Figure 10. Integrated velocity channel contours (in red) of $\text{C}^{18}\text{O}(J=2-1)$ emission (at velocity intervals of 1 km s^{-1}) toward an area containing i17008 and i17009. The contour levels are 1.5, 2.4, 3.5, 5.5, 7.5, 9, 12, and 13 K km s^{-1} . The scale bar and other symbols are the same as in Figure 7a. In each panel, a filled circle shows the location of the MIR bubble S11.

explanation of the origin of ionized filaments is likely due to the feedback from massive stars.

Most recently, Whitworth & Priestley (2021) studied a semi-analytic model concerning ionizing feedback from an O star formed in a filament. According to the model, the filament is generally destroyed by the ionizing radiation from the O star, and the ionized gas disperses freely into the surroundings. We refer to this as a “case-I” phase in this work. In the case of relatively wide and/or relatively dense filament and/or low the rate at which the O star emits ionizing photons, the ongoing accretion inflow on to the filament will reduce the escape of ionized gas, and might trap the ionizing radiation from the O star. This will slow the erosion of the filament, and the model also shows the formation of a relatively dense, compact, and

turbulent H II region around the ionizing stars. We refer to this as a “case-II” phase.

The spatial association of molecular gas with the ionized structures seems to indicate that the filamentary molecular clouds are pre-existing structures (see Figures 2 and 4). Hence, the filamentary molecular clouds are unlikely to be formed by the feedback of young massive OB stars associated with the ionized filaments. However, the energetics of massive stars appear to have influenced their parent filamentary molecular clouds (see Figures 2 and 4). In other words, massive stars wreak havoc on the gas and dust in the parental filamentary molecular clouds.

The knowledge of three pressure components (i.e., pressure of an H II region (P_{HII}), radiation pressure (P_{rad}), and stellar wind

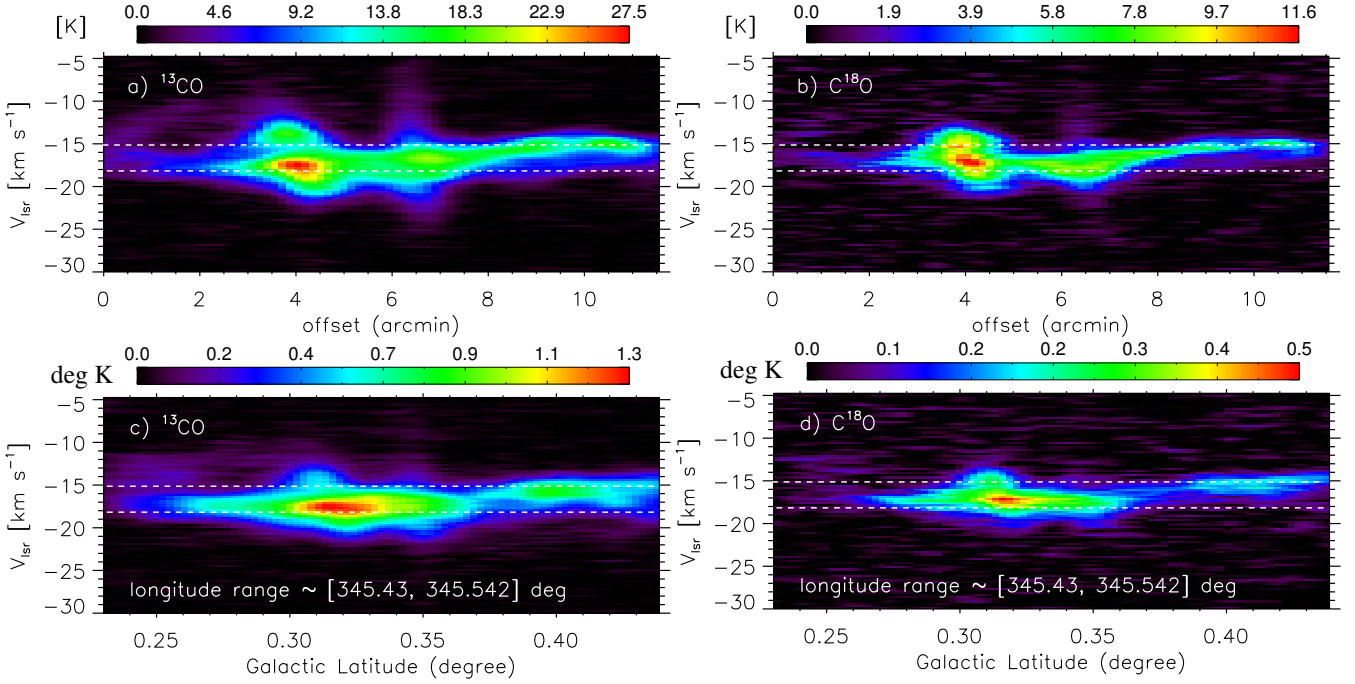


Figure 11. Position-velocity diagram of a) $^{13}\text{CO}(J=2-1)$; b) $\text{C}^{18}\text{O}(J=2-1)$ along the curve highlighted in Figures 7a and 7d. Latitude-velocity diagram of c) $^{13}\text{CO}(J=2-1)$; d) $\text{C}^{18}\text{O}(J=2-1)$. The molecular emission is integrated over a longitude range, which is indicated in panels “c” and “d”. In all panels, the horizontal dashed lines (in white) are shown at $V_{\text{lsr}} = -18$ and -15 km s^{-1} .

ram pressure (P_{wind}) driven by a massive OB star can be useful to explore the feedback of a massive star in its vicinity (e.g., Dewangan et al. 2016a). The equations of different pressure components are $P_{\text{HII}} = \mu m_H c_s^2 \left(\sqrt{\frac{3N_{\text{UV}}}{4\pi\alpha_B D_s^3}} \right)$; $P_{\text{rad}} = L_{\text{bol}}/4\pi c D_s^2$; and $P_{\text{wind}} = \dot{M}_w V_w / 4\pi D_s^2$ (see Bressert et al. 2012; Dewangan et al. 2016a, for more details). In these equations, N_{UV} is defined earlier, c_s is the sound speed of the photo-ionized gas (i.e., 11 km s^{-1} ; Bisbas et al. 2009), α_B is the radiative recombination coefficient ($= 2.6 \times 10^{-13} \times (10^4 \text{ K}/T_e)^{0.7} \text{ cm}^3 \text{ s}^{-1}$; see Kwan 1997), μ is the mean molecular weight in the ionized gas (i.e., 0.678; Bisbas et al. 2009), m_H is the hydrogen atom mass, \dot{M}_w is the mass-loss rate, V_w is the wind velocity of the ionizing source, L_{bol} is the bolometric luminosity of the source, and D_s is the projected distance from the position of a massive star where the pressure components are determined.

In the case of Wolf-Rayet stars, the value of P_{wind} dominates over the values of P_{HII} and P_{rad} (e.g., Lamers & Cassinelli 1999; Dewangan et al. 2016b; Baug et al. 2019). But, the value of P_{HII} driven by massive zero age main sequence stars often exceeds their P_{rad} and P_{wind} components (e.g., Dewangan et al. 2016a). Hence, we have computed only the values of P_{HII} in the direction of IF-A and IF-B. We find a total of $N_{\text{uv}} = 1.72 \times 10^{48} \text{ s}^{-1}$ of three clumps “A–C” in IF-A, while a total of $N_{\text{uv}} = 2.65 \times 10^{48} \text{ s}^{-1}$ of three clumps “E–G” in IF-B are estimated. Considering the elongated appearance of the filaments, we choose a value of $D_s = 3 \text{ pc}$ for the calculations. Using $\alpha_B = 2.6 \times 10^{-13} \text{ cm}^3 \text{ s}^{-1}$ at $T_e = 10^4 \text{ K}$ and $D_s = 3 \text{ pc}$, we calculated the values of P_{HII} to be $\approx 6.1 \times 10^{-11}$ and $\approx 7.6 \times 10^{-11} \text{ dynes cm}^{-2}$ for IF-A and IF-B, respectively. Each value can be compared with the pressure exerted by the self-gravity of the surrounding molecular gas around respective ionized filament. Based on the detection of various molecular emission (e.g., C^{18}O (critical density $\sim 10^4 \text{ cm}^{-3}$); see Figures 3 and 5), we assume the

values of particle density $\geq 10^4 \text{ cm}^{-3}$ for IF-A, and $< 10^3 \text{ cm}^{-3}$ for IF-B. From Table 7.3 in Dyson & Williams (1997), we find pressure values (P_{MC}) for typical cool molecular clouds (particle density $\sim 10^3 - 10^4 \text{ cm}^{-3}$ and temperature $\sim 20 \text{ K}$) to be $\sim 2.8 \times 10^{-12} - 2.8 \times 10^{-11} \text{ dynes cm}^{-2}$.

Concerning the parent molecular cloud of IF-A, an H II region powered by a massive star is traced at its three different locations. In other words, there are three H II regions toward the parent molecular cloud of IF-A. The combined feedback of three H II regions located in the elongated molecular cloud has not eroded the parent cloud, and may be responsible for the elongated ionized morphology of IF-A. It is supported by the pressure values (i.e., $P_{\text{HII}} \approx P_{\text{MC}}$) inferred toward IF-A. On the basis of the C^{18}O emission and the dust continuum emission, we consider the parent molecular cloud of IF-A as a dense filament. Therefore, the filamentary cloud associated with IF-A resembles the “case-II” phase as described by Whitworth & Priestley (2021).

In a similar fashion, the existence of IF-B may be explained by the combined feedback of massive stars powering the ionized clumps “D–G”. Furthermore, the central part of the parent molecular cloud of IF-B hosts bubble-like structures (with $T_d = 21\text{--}27 \text{ K}$) as seen in the *Herschel* temperature map, and seems to be destroyed by the impact of the H II regions in the ionized filament IF-B. In this relation, one may also obtain the hint from the pressure values (i.e., $P_{\text{HII}} > P_{\text{MC}}$) in IF-B. After the erosion of the filamentary molecular cloud, the ionizing radiation has freely streamed out, which could lead to the elongated ionized morphology of IF-B. This implies the applicability of the “case-I” phase as reported by Whitworth & Priestley (2021).

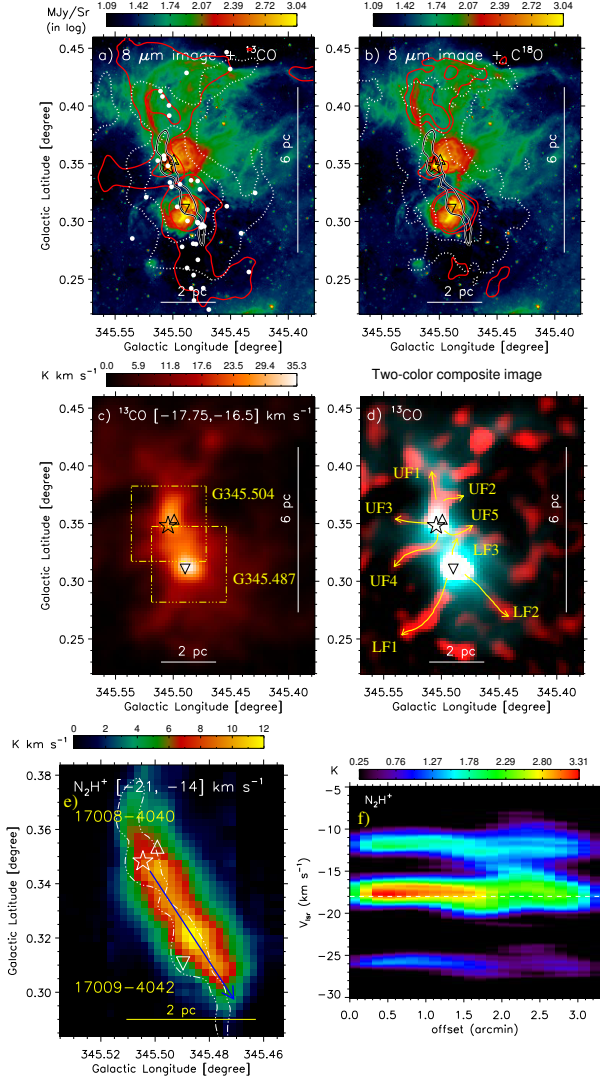


Figure 12. Different cloud components toward an area containing i17008 and i17009. a) Overlay of the $^{13}\text{CO}(J=2-1)$ emission of two clouds and the positions of previously reported YSOs (see filled white circles; from Dewangan et al. 2018c) on the *Spitzer* 8.0 μm image. The molecular emission at $[-15.25, -11] \text{ km s}^{-1}$ is shown by solid red contours with the levels of $[5.35, 15.86] \text{ K km s}^{-1}$. The dotted contours (in white) are the molecular emission at $[-22.25, -16] \text{ km s}^{-1}$ with the levels of $[14, 33.16] \text{ K km s}^{-1}$. b) Overlay of the $\text{C}^{18}\text{O}(J=2-1)$ emission of two clouds on the *Spitzer* 8.0 μm image. The molecular emission at $[-15.25, -11] \text{ km s}^{-1}$ is shown by solid red contours with the levels of $[2.2, 19.42] \text{ K km s}^{-1}$. The dotted contours (in white) are the molecular emission at $[-22.25, -16] \text{ km s}^{-1}$ with the levels of $[2.5, 41.72] \text{ K km s}^{-1}$. c) The intensity map of $^{13}\text{CO}(J=2-1)$ integrated over a velocity range of $[-17.75, -16.5] \text{ km s}^{-1}$. The areas covered by the MALT90 survey toward G345.504/i17008 and G345.487/i17009 are indicated by dotted-dashed boxes (see also Figure 12e). d) The panel displays a two-color composite map made using the $^{13}\text{CO}(J=2-1)$ maps. In the color-composite image, the “Edge-DoG” processed $^{13}\text{CO}(J=2-1)$ map at $[-17.75, -16.5] \text{ km s}^{-1}$ is presented in red color, while the $^{13}\text{CO}(J=2-1)$ map at $[-24, -9] \text{ km s}^{-1}$ is shown in turquoise color. Based on visual inspection, eight curves are marked and labeled in the panel. e) Intensity map of the molecule $\text{N}_2\text{H}^+(1-0)$ (from MALT90 data set) integrated over a velocity range of $[-21, -14] \text{ km s}^{-1}$. f) Position-velocity diagram of $\text{N}_2\text{H}^+(1-0)$ along an arrow as highlighted in the $\text{N}_2\text{H}^+(1-0)$ map (see Figure 12e). The position-velocity map of N_2H^+ was smoothed with a Gaussian function with a width of 3 pixels. A horizontal line at $V_{\text{LSR}} = -18 \text{ km s}^{-1}$ is also indicated in the panel. In each panel (except panel “f”), the scale bar and other symbols are the same as in Figure 7a. In panels “a” and “b”, a black curve highlights the elongated filament.

MNRAS **000**, 1–?? (2020)

4.3 Velocity structure function toward IF-A

It is possible that the colliding filaments and the stellar feedback from massive stars may drive internal turbulence in the parent clouds of both the ionized filaments. In this section, to examine the properties of turbulence, we study the velocity structure function of a continuous elongated molecular structure associated with IF-A. In this connection, we determined the second-order structure function ($S_2(L)$) as reported in Hacar et al. (2016), and the square root of the second-order structure function is defined as:

$$S_2(L)^{1/2} = \delta V = \langle |V(r) - V(r+L)|^2 \rangle^{1/2} = \langle |\delta u_l|^2 \rangle^{1/2} \quad (3)$$

Here, $\delta u_l = V(r) - V(r+L)$ is the velocity difference between two positions separated by a lag. Based on the earlier reported work by Heyer & Brunt (2004), we find that the velocity structure function defined in this way is a useful tool to study properties of turbulence in molecular clouds and can be directly compared with the Larson’s size-linewidth relation (Larson 1981).

In this work, the structure functions are derived from the ^{13}CO and N_2H^+ line data. The lines with different critical densities give an opportunity to study gas dynamics in less dense (extended) and more dense (compact) parts of the filament. Line velocities are determined from Gaussian fitting to the profiles.

Using the ^{13}CO line data, structure functions are constructed for two different velocity ranges of $[-19, -17] \text{ km s}^{-1}$ and $[-16, -14] \text{ km s}^{-1}$ as presented in Figures 13a and 13b, respectively. In the calculations, the ^{13}CO integrated intensities ($I(^{13}\text{CO})$) $> 3 \text{ K km s}^{-1}$ and a lag of $20''$ are considered. A range of linewidth of $[1, 3] \text{ km s}^{-1}$ is adopted in order to exclude the spectra with overlapping components in the analysis.

The N_2H^+ line data are known to trace dense gas in a given star-forming region. Therefore, to study structure functions toward the dense clumps hosting IRAS 17008-4040/G345.504 and IRAS 17009-4042/G345.487, the N_2H^+ line data are employed. Using the N_2H^+ line data, Figures 13c and 13d present structure functions for an area hosting IRAS 17008-4040/G345.504 and IRAS 17009-4042/G345.487, respectively. The calculations use a velocity range of $[-19, -17] \text{ km s}^{-1}$, a lag of $10''$, and a range of linewidth of $[1, 3] \text{ km s}^{-1}$.

In general, concerning the study of turbulence in molecular clouds, the Larson’s one-dimensional velocity dispersion-size relationship or Larson’s scaling relation (i.e., $\delta V = 0.63 \times L^{0.38}$; Larson 1981) can be examined. In this relation, one can expect the dominant turbulent flow against the kinematically coupled large-scale, ordered motion in molecular clouds. Using the ^{13}CO line data, Hacar et al. (2016) studied the velocity structure function for the Musca cloud (i.e., $\delta V = 0.38 \times L^{0.58}$), which was found to be different from the Larson’s scaling relation. This deviation was attributed due to the presence of sonic-like structure in the cloud which is decoupled with the dominant turbulent velocity structure.

In Figures 13a–13d, we have also shown the Larson’s scaling (i.e., $\delta V = 0.63 \times L^{0.38}$), the relation concerning the star-forming site S242 (i.e., $\delta V = 0.42 \times L^{0.48}$; Dewangan et al. 2019b), and a relationship of the Musca cloud (i.e., $\delta V = 0.38 \times L^{0.58}$) by dashed blue line, solid black line, and dashed red line, respectively.

Structure functions of the selected regions show nearly power-law dependencies for lower L ($\leq 2 \text{ pc}$ using ^{13}CO and ≤ 0.5 – 1 pc using N_2H^+ ; see the X-axis in Figure 13). For higher L , structure functions behave mostly in an irregular manner. In Figures 13a–13d, all the structure functions as those for S242 and Musca lie under the Larson’s dependence. The power-law dependencies of the structure functions using the ^{13}CO $[-16, -14] \text{ km s}^{-1}$ (see Figure 13b)

and for the region G345.487 using the N_2H^+ line data (see Figure 13d) turn out to be close to the one, which is also found for S242 having a power-law index of about 0.48. A power-law index of the structure function derived from the ^{13}CO $[-19, -17]$ km s^{-1} data is about 0.6. These indices are higher than of the Larson's dependence, and are predicted for supersonic incompressible turbulence with intermittency (e.g., She & Leveque 1994; Boldyrev 2002). In order to compare our estimated indices with the predictions of the highlighted papers, one has to multiply our indices by 2 as we used a square root of the structure function. Furthermore, using the ^{13}CO line data, we also compared the structure functions derived for the inner subregion containing the filament against its surrounding (outer) gas. For the ^{13}CO $[-16, -14]$ km s^{-1} range, no definite differences in the power-law indices are found. However, for the ^{13}CO $[-19, -17]$ km s^{-1} range, the index of the power-law dependence in surrounding gas is higher than for the filament (see Figures 13e and 13f).

Chira et al. (2019) studied the evolution of simulated turbulent clouds under the influence of various physical processes and explored how velocity structure functions change with time. Their results show a general behavior of the structure function-L dependencies similar to ours (Figures 13a–13d) at early stages of the cloud evolution. The power-law indices of their structure function-L without density weighting – which is our case – appear to be higher than the theoretical predictions in accordance with our results. It is also found that the structure function's power-law indices decrease with time due to growing influence of systemic velocities in self-gravitating gas on small scales. In the direction of the ionized filament IF-A, different scales of the regions, where turbulence dominates as observed from the ^{13}CO and N_2H^+ structure functions, are most likely due to the difference in critical densities of these molecular lines. The difference in the power-law indices of the structure function dependencies calculated using the ^{13}CO $[-19, -17]$ km s^{-1} data for the region of the filament and for its surrounding gas could reflect the difference in turbulent properties connected with the feedback from massive stars in the filament.

We conclude that the observed power-law dependencies of the structure functions derived from molecular line data for the ionized filament IF-A most probably reflect turbulent properties of gas. In order to confirm the properties of turbulence in massive star-forming cores, which differ from their surroundings, new observations with high sensitivity and high angular resolution using the lines with different critical densities are needed. Using the line data, the study of velocity structure functions, and their comparison with the theoretical predictions and the results of model simulations seems to be a useful tool for this purpose.

5 SUMMARY AND CONCLUSIONS

To observationally investigate the embedded morphology and ongoing physical mechanisms around $l = 345^\circ.5$, we have carried an analysis of multi-wavelength data of an area of $\sim 74'.6 \times 55'$. The radio continuum map at 843 MHz reveals two distinct ionized filaments (i.e., IF-A (extent $\sim 8'.5$) and IF-B (extent $\sim 22'.65$)). Ionized clumps powered by massive OB stars are identified toward both the ionized filaments. The $^{13}\text{CO}(1-0)$, $^{13}\text{CO}(2-1)$, and $\text{C}^{18}\text{O}(2-1)$ emissions are examined in a velocity range of $[-21, -10]$ km s^{-1} to study the parent molecular clouds of IF-A and IF-B, which have filamentary appearances. However, IF-A and IF-B seem to be situated at a distance of 2.4 kpc and 1.4 kpc, respectively. We have investigated two cloud components around -18 and -15 km s^{-1}

toward the filamentary parent clouds of IF-A and IF-B, which are connected in velocity space. The filamentary cloud components also spatially overlap with each other along the major axis, which may be treated as filamentary twisting/coupling. Massive stars are evident toward the common zones of the cloud components, where noticeable Class I protostars also seem to be present. Based on our observational outcomes, we suggest the possibility of the collision of two filamentary clouds around 1.2 Myr ago. The origin of IF-A and IF-B may be explained by the combined feedback of massive stars.

The continuous elongated structure of the parent cloud of IF-A is identified in the molecular maps, and power-law dependencies of its structure functions are found, reflecting turbulent properties of gas. The difference in the power-law indices of the structure function dependencies for the gas in the filament and its surrounding gas is found. It could be connected with the influence of massive stars on the filament, which may affect the turbulent properties.

The central part of the parent cloud of IF-B is broken where this ionized filament is detected. Considering the observed ionized and molecular morphologies, our results seem to support the findings of the most recent model of Whitworth & Priestley (2021), which is related to the escape and the trap of the ionizing radiation from an O star formed in a filament.

ACKNOWLEDGMENTS

We are grateful to the anonymous reviewer for the constructive comments and suggestions. The research work at Physical Research Laboratory is funded by the Department of Space, Government of India. L.E.P. acknowledges the support of the IAP State Program 0030-2021-0005. This work is based [in part] on observations made with the *Spitzer* Space Telescope, which is operated by the Jet Propulsion Laboratory, California Institute of Technology under a contract with NASA. This publication is based on data acquired with the Atacama Pathfinder Experiment (APEX) under programmes 092.F-9315 and 193.C-0584. APEX is a collaboration among the Max-Planck-Institut für Radioastronomie, the European Southern Observatory, and the Onsala Space Observatory. The processed data products are available from the SEDIGISM survey database located at <https://sedigism.mpifr-bonn.mpg.de/index.html>, which was constructed by James Urquhart and hosted by the Max Planck Institute for Radio Astronomy. A part of this work has made use of data from the European Space Agency (ESA) mission Gaia, processed by the Gaia Data Processing and Analysis Consortium (DPAC). Funding for the DPAC is provided by national institutions, in particular, the institutions participating in the Gaia Multilateral Agreement.

Data availability

Distances to stars in the GAIA EDR3 underlying this article are available from the publicly accessible website¹. The *Herschel*, WISE, and *Spitzer* data underlying this article are available from the publicly accessible NASA/IPAC infrared science archive². The *Herschel* temperature map underlying this article is available from the publicly accessible website³. The ATLASGAL 870 μm continuum

¹ <https://cdsarc.cds.unistra.fr/viz-bin/cat/I/352>

² <https://irsa.ipac.caltech.edu/frontpage/>

³ <http://www.astro.cardiff.ac.uk/research/ViaLactea/>

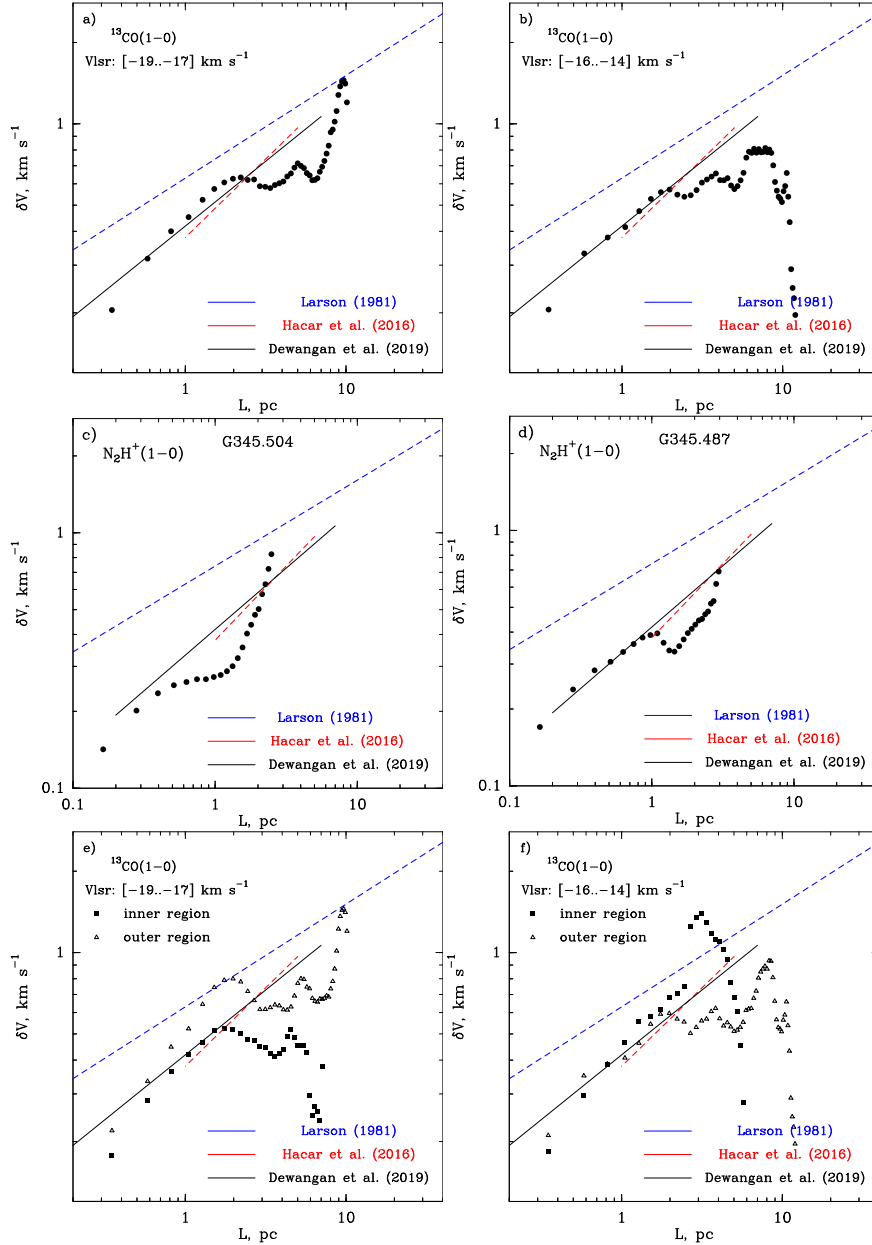


Figure 13. All the panels show a structure function in velocity δV as a function of length. a) The structure function is derived using the ^{13}CO line data for a velocity range of $[-19, -17] \text{ km s}^{-1}$ and for the total area containing the molecular filamentary region associated with IF-A (see Figure 7a). b) The structure function is generated using the ^{13}CO line data for a velocity range of $[-16, -14] \text{ km s}^{-1}$ (see Figure 7a). c) The structure function is produced using the N_2H^+ line data for an area related to G345.504 (see Figure 12c). d) The structure function is derived using the N_2H^+ line data for an area related to G345.487 (see Figure 12c). e) The structure function is computed using the ^{13}CO line data for a velocity range of $[-19, -17] \text{ km s}^{-1}$ and for an area located within (i.e., inner/filamentary region; see filled squares) and outside (outer region; see open triangles) of the ^{13}CO contour as shown in Figure 7a. f) The structure function is computed using the ^{13}CO line data for a velocity range of $[-16, -14] \text{ km s}^{-1}$ and for inner regions (see filled squares) and outer regions (see open triangles) of the filament. In panels “c” and “d”, line velocities lie within a velocity range of $[-19, -17] \text{ km s}^{-1}$. In each panel, the Larson’s velocity dispersion-size relationship (i.e., $\delta V = 0.63 \times L^{0.38}$; Larson 1981) is marked by a dashed blue line. In all panels, a solid black line shows the relation, $\delta V = 0.42 \times L^{0.48}$ related to the star-forming site S242 (from Dewangan et al. 2019b). In each panel, the velocity dispersion-size relationship of the Musca cloud is highlighted by a dashed red line (e.g., $\delta V = 0.38 \times L^{0.58}$; Hacar et al. 2016). A lag corresponds to $20''$ and $10''$ for the areas using the ^{13}CO and N_2H^+ line data, respectively.

data underlying this article are available from the publicly accessible ATLASGAL database server⁴. The SEDIGISM molecular line data underlying this article are available from the publicly accessi-

ble website⁵. The Mopra molecular line data underlying this article are available from the publicly accessible website⁶. The MALT90

⁴ <https://www3.mpifr-bonn.mpg.de/div/atlasgal/>

⁵ https://sedigism.mpifr-bonn.mpg.de/cgi-bin-seg/SEDIGISM_DATABASE.cgi

⁶ <https://dataverse.harvard.edu/dataset.xhtml?persistentId=doi:10.7910/DVN/LH3BDN>

molecular line data underlying this article are available from the publicly accessible website⁷. The SUMSS 843 MHz continuum data underlying this article are available from the publicly accessible server⁸.

REFERENCES

- Ananthpindika S. V., 2010, *MNRAS*, **405**, 1431
- André P., et al., 2010, *A&A*, **518**, L102
- André P., Di Francesco J., Ward-Thompson D., Inutsuka S. I., Pudritz R. E., Pineda J. E., 2014, in Beuther H., Klessen R. S., Dullemond C. P., Henning T., eds, *Protostars and Planets VI*. p. 27 ([arXiv:1312.6232](#)), [doi:10.2458/azu_uapress_9780816531240-ch002](#)
- Assirati L., Silva N. R., Berton L., Lopes A. A., Bruno O. M., 2014, in *Journal of Physics Conference Series*. p. 012020 ([arXiv:1311.2561](#)), [doi:10.1088/1742-6596/490/1/012020](#)
- Bailer-Jones C. A. L., Rybizki J., Fousneau M., Demleitner M., Andrae R., 2021, *AJ*, **161**, 147
- Balfour S. K., Whitworth A. P., Hubber D. A., Jaffa S. E., 2015, *MNRAS*, **453**, 2471
- Balfour S. K., Whitworth A. P., Hubber D. A., 2017, *MNRAS*, **465**, 3483
- Baug T., de Grijs R., Dewangan L. K., Herczeg G. J., Ojha D. K., Wang K., Deng L., Bhatt B. C., 2019, *ApJ*, **885**, 68
- Beltrán M. T., Rivilla V. M., Kumar M. S. N., Cesaroni R., Galli D., 2022, *A&A*, **660**, L4
- Benjamin R. A., et al., 2003, *PASP*, **115**, 953
- Bisbas T. G., Wünsch R., Whitworth A. P., Hubber D. A., 2009, *A&A*, **497**, 649
- Bisbas T. G., Tanaka K. E. I., Tan J. C., Wu B., Nakamura F., 2017, *ApJ*, **850**, 23
- Bock D. C. J., Large M. I., Sadler E. M., 1999, *AJ*, **117**, 1578
- Boldyrev S., 2002, *ApJ*, **569**, 841
- Braiding C., et al., 2018, *Publ. Astron. Soc. Australia*, **35**, e029
- Bressert E., Ginsburg A., Bally J., Battersby C., Longmore S., Testi L., 2012, *ApJ*, **758**, L28
- Carey S. J., et al., 2005, in *American Astronomical Society Meeting Abstracts*. p. 63.33
- Chira R. A., Ibáñez-Mejía J. C., Mac Low M. M., Henning T., 2019, *A&A*, **630**, A97
- Churchwell E., et al., 2006, *ApJ*, **649**, 759
- Cyganowski C. J., et al., 2008, *AJ*, **136**, 2391
- Dewangan L. K., 2022, arXiv e-prints, [p. arXiv:2204.02127](#)
- Dewangan L. K., Ojha D. K., 2017, *ApJ*, **849**, 65
- Dewangan L. K., Ojha D. K., Luna A., Anandarao B. G., Ninan J. P., Mallick K. K., Mayya Y. D., 2016a, *ApJ*, **819**, 66
- Dewangan L. K., Baug T., Ojha D. K., Janardhan P., Ninan J. P., Luna A., Zinchenko I., 2016b, *ApJ*, **826**, 27
- Dewangan L. K., Ojha D. K., Zinchenko I., Janardhan P., Luna A., 2017a, *ApJ*, **834**, 22
- Dewangan L. K., Ojha D. K., Baug T., 2017b, *ApJ*, **844**, 15
- Dewangan L. K., Ojha D. K., Zinchenko I., Baug T., 2018a, *ApJ*, **861**, 19
- Dewangan L. K., Dhanya J. S., Ojha D. K., Zinchenko I., 2018b, *ApJ*, **866**, 20
- Dewangan L. K., Baug T., Ojha D. K., Ghosh S. K., 2018c, *ApJ*, **869**, 30
- Dewangan L. K., Ojha D. K., Baug T., Devaraj R., 2019a, *ApJ*, **875**, 138
- Dewangan L. K., Pirogov L. E., Ryabukhina O. L., Ojha D. K., Zinchenko I., 2019b, *ApJ*, **877**, 1
- Dewangan L. K., Dhanya J. S., Bhadani N. K., Ojha D. K., Baug T., 2021, *MNRAS*, **506**, 6081
- Dhanya J. S., Dewangan L. K., Ojha D. K., Mandal S., 2021, *PASJ*, **73**, S355
- Dyson J. E., Williams D. A., 1997, *The physics of the interstellar medium*, [doi:10.1201/9780585368115](#).
- Emig K. L., et al., 2022, arXiv e-prints, [p. arXiv:2205.09193](#)
- Enokiya R., Torii K., Fukui Y., 2021, *PASJ*, **73**, S75
- Evans Neal J. I., et al., 2009, *ApJS*, **181**, 321
- Fabircius C., et al., 2021, *A&A*, **649**, A5
- Foster J. B., et al., 2011, *ApJS*, **197**, 25
- Fukui Y., et al., 2014, *ApJ*, **780**, 36
- Fukui Y., et al., 2018, *ApJ*, **859**, 166
- Fukui Y., et al., 2019, *ApJ*, **886**, 14
- Fukui Y., Habe A., Inoue T., Enokiya R., Tachihara K., 2021, *PASJ*, **73**, S1
- Gaczowski B., et al., 2015, *A&A*, **584**, A36
- Gaczowski B., et al., 2017, *A&A*, **608**, A102
- Gaia Collaboration et al., 2021, *A&A*, **649**, A1
- Garay G., Brooks K. J., Mardones D., Norris R. P., 2006, *ApJ*, **651**, 914
- Garay G., Mardones D., Brooks K. J., Videla L., Contreras Y., 2007, *ApJ*, **666**, 309
- Getman K. V., Feigelson E. D., Garmire G., Broos P., Wang J., 2007, *ApJ*, **654**, 316
- Gonzalez R. C., Woods R. E., 2002, *Digital image processing*, 2nd edn. Prentice-Hall, Englewood Cliffs, NJ
- Habe A., Ohta K., 1992, *PASJ*, **44**, 203
- Hacar A., Kainulainen J., Tafalla M., Beuther H., Alves J., 2016, *A&A*, **587**, A97
- Hanaoka M., et al., 2020, *PASJ*, **72**, 5
- Hartmann L., Megeath S. T., Allen L., Luhman K., Calvet N., D'Alessio P., Franco-Hernandez R., Fazio G., 2005, *ApJ*, **629**, 881
- Haworth T. J., et al., 2015a, *MNRAS*, **450**, 10
- Haworth T. J., Shima K., Tasker E. J., Fukui Y., Torii K., Dale J. E., Takahira K., Habe A., 2015b, *MNRAS*, **454**, 1634
- Henshaw J. D., Caselli P., Fontani F., Jiménez-Serra I., Tan J. C., Hernandez A. K., 2013, *MNRAS*, **428**, 3425
- Heyer M. H., Brunt C. M., 2004, *ApJ*, **615**, L45
- Hirota T., 2018, *Publication of Korean Astronomical Society*, **33**, 21
- Inoue T., Fukui Y., 2013, *ApJ*, **774**, L31
- Inoue T., Hennebelle P., Fukui Y., Matsumoto T., Iwasaki K., Inutsuka S.-i., 2018, *PASJ*, **70**, S53
- Jackson J. M., et al., 2013, *Publ. Astron. Soc. Australia*, **30**, e057
- Karr J. L., Martin P. G., 2003, *ApJ*, **595**, 880
- Kohno M., et al., 2018, *PASJ*, **70**, S50
- Krause M. G. H., et al., 2018, *A&A*, **619**, A120
- Kwan J., 1997, *ApJ*, **489**, 284
- Lamers H. J. G. L. M., Cassinelli J. P., 1999, *Introduction to Stellar Winds*
- Larson R. B., 1981, *MNRAS*, **194**, 809
- Liang X., Xu J.-L., Xu Y., Wang J.-J., 2021, *ApJ*, **913**, 14
- Marsh K. A., Whitworth A. P., Lomax O., 2015, *MNRAS*, **454**, 4282
- Marsh K. A., et al., 2017, *MNRAS*, **471**, 2730
- Matsakis D. N., Evans N. J. I., Sato T., Zuckerman B., 1976, *AJ*, **81**, 172
- Molinari S., et al., 2010a, *PASP*, **122**, 314
- Molinari S., et al., 2010b, *A&A*, **518**, L100
- Morales E. F. E., Mardones D., Garay G., Brooks K. J., Pineda J. E., 2009, *ApJ*, **698**, 488
- Motte F., Bontemps S., Louvet F., 2018, *ARA&A*, **56**, 41
- Myers P. C., 2009, *ApJ*, **700**, 1609
- Panagia N., 1973, *AJ*, **78**, 929
- Pon A., Johnstone D., Bally J., Heiles C., 2014, *MNRAS*, **441**, 1095
- Priestley F. D., Whitworth A. P., 2021, *MNRAS*, **506**, 775
- Rosen A. L., Offner S. S. R., Sadavoy S. I., Bhandare A., Vázquez-Semadeni E., Ginsburg A., 2020, *Space Sci. Rev.*, **216**, 62
- Schuller F., et al., 2009, *A&A*, **504**, 415
- Schuller F., et al., 2017, *A&A*, **601**, A124
- Schuller F., et al., 2021, *MNRAS*, **500**, 3064
- She Z.-S., Leveque E., 1994, *Phys. Rev. Lett.*, **72**, 336
- Tan J. C., Beltrán M. T., Caselli P., Fontani F., Fuente A., Krumholz M. R., McKee C. F., Stolte A., 2014, in Beuther H., Klessen R. S., Dullemond C. P., Henning T., eds, *Protostars and Planets VI*. p. 149 ([arXiv:1402.0919](#)), [doi:10.2458/azu_uapress_9780816531240-ch007](#)
- Tigé J., et al., 2017, *A&A*, **602**, A77
- Torii K., et al., 2011, *ApJ*, **738**, 46
- Torii K., et al., 2015, *ApJ*, **806**, 7

⁷ <http://malt90.bu.edu/>

⁸ <https://skyview.gsfc.nasa.gov/current/cgi/query.pl>

- Torii K., et al., 2017, [ApJ](#), **835**, 142
Treviño-Morales S. P., et al., 2019, [A&A](#), **629**, A81
Urquhart J. S., et al., 2018, [MNRAS](#), **473**, 1059
Watson C., Hanspal U., Mengistu A., 2010, [ApJ](#), **716**, 1478
Whitworth A. P., Priestley F. D., 2021, [MNRAS](#), **504**, 3156
Williams J. P., de Geus E. J., Blitz L., 1994, [ApJ](#), **428**, 693
Wright E. L., et al., 2010, [AJ](#), **140**, 1868
Yang A. Y., et al., 2022, [A&A](#), **658**, A160